THE EUROPEAN
PHYSICAL JOURNAL C

Production of pions, kaons and protons in pp collisions at $\sqrt{s} = 900$ GeV with ALICE at the LHC

The ALICE Collaboration

K. Aamodt[77], N. Abel[43], U. Abeysekara[75], A. Abrahantes Quintana[42], A. Abramyan[112], D. Adamová[85],
M.M. Aggarwal[25], G. Aglieri Rinella[40], A.G. Agocs[18], S. Aguilar Salazar[63], Z. Ahammed[53], A. Ahmad[2], N. Ahmad[2],
S.U. Ahn[38,b], R. Akimoto[99], A. Akindinov[66], D. Aleksandrov[68], B. Alessandro[104], R. Alfaro Molina[63], A. Alici[13],
E. Almaráz Aviña[63], J. Alme[8], T. Alt[43,c], V. Altini[5], S. Altinpinar[31], C. Andrei[17], A. Andronic[31], G. Anelli[40],
V. Angelov[43,c], C. Anson[27], T. Antičić[113], F. Antinori[40,d], S. Antinori[13], K. Antipin[36], D. Antończyk[36], P. Antonioli[14],
A. Anzo[63], L. Aphecetche[71], H. Appelshäuser[36], S. Arcelli[13], R. Arceo[63], A. Arend[36], N. Armesto[91], R. Arnaldi[104],
T. Aronsson[72], I.C. Arsene[77,e], A. Asryan[97], A. Augustinus[40], R. Averbeck[31], T.C. Awes[74], J. Äystö[49], M.D. Azmi[2],
S. Bablok[8], M. Bach[35], A. Badalà[24], Y.W. Baek[38,b], S. Bagnasco[104], R. Bailhache[31,f], R. Bala[103], A. Baldisseri[88],
A. Baldit[26], J. Bán[56], R. Barbera[23], G.G. Barnaföldi[18], L.S. Barnby[12], V. Barret[26], J. Bartke[29], F. Barile[5],
M. Basile[13], V. Basmanov[93], N. Bastid[26], B. Bathen[70], G. Batigne[71], B. Batyunya[34], C. Baumann[70,f], I.G. Bearden[28],
B. Becker[20,g], I. Belikov[98], R. Bellwied[33], E. Belmont-Moreno[63], A. Belogianni[4], L. Benhabib[71], S. Beole[103],
I. Berceanu[17], A. Bercuci[31,h], E. Berdermann[31], Y. Berdnikov[39], L. Betev[40], A. Bhasin[48], A.K. Bhati[25], L. Bianchi[103],
N. Bianchi[37], C. Bianchin[78], J. Bielčík[80], J. Bielčíková[85], A. Bilandzic[3], L. Bimbot[76], E. Biolcati[103], A. Blanc[26],
F. Blanco[23,i], F. Blanco[61], D. Blau[68], C. Blume[36], M. Boccioli[40], N. Bock[27], A. Bogdanov[67], H. Bøggild[28],
M. Bogolyubsky[82], J. Bohm[95], L. Boldizsár[18], M. Bombara[55], C. Bombonati[78,k], M. Bondila[49], H. Borel[88],
A. Borisov[50], C. Bortolin[78,ao], S. Bose[52], L. Bosisio[100], F. Bossú[103], M. Botje[3], S. Böttger[43], G. Bourdaud[71],
B. Boyer[76], M. Braun[97], P. Braun-Munzinger[31,32,c], L. Bravina[77], M. Bregant[100,l], T. Breitner[43], G. Bruckner[40],
R. Brun[40], E. Bruna[72], G.E. Bruno[5], D. Budnikov[93], H. Buesching[36], P. Buncic[40], O. Busch[44], Z. Buthelezi[22],
D. Caffarri[78], X. Cai[111], H. Caines[72], E. Calvo[58], E. Camacho[64], P. Camerini[100], M. Campbell[40], V. Canoa Roman[40],
G.P. Capitani[37], G.Cara Romeo[14], F. Carena[40], W. Carena[40], F. Carminati[40], A. Casanova Díaz[37], M. Caselle[40],
J. Castillo Castellanos[88], J.F. Castillo Hernandez[31], V. Catanescu[17], E. Cattaruzza[100], C. Cavicchioli[40], P. Cerello[104],
V. Chambert[76], B. Chang[95], S. Chapeland[40], A. Charpy[76], J.L. Charvet[88], S. Chattopadhyay[52], S. Chattopadhyay[53],
M. Cherney[75], C. Cheshkov[40], B. Cheynis[106], E. Chiavassa[103], V. Chibante Barroso[40], D.D. Chinellato[21],
P. Chochula[40], K. Choi[84], M. Chojnacki[105], P. Christakoglou[105], C.H. Christensen[28], P. Christiansen[60], T. Chujo[102],
F. Chuman[45], C. Cicalo[20], L. Cifarelli[13], F. Cindolo[14], J. Cleymans[22], O. Cobanoglu[103], J.-P. Coffin[98], S. Coli[104],
A. Colla[40], G. Conesa Balbastre[37], Z. Conesa del Valle[71,m], E.S. Conner[110], P. Constantin[44], G. Contin[100,k],
J.G. Contreras[64], Y. Corrales Morales[103], T.M. Cormier[33], P. Cortese[1], I. Cortés Maldonado[83], M.R. Cosentino[21],
F. Costa[40], M.E. Cotallo[61], E. Crescio[64], P. Crochet[26], E. Cuautle[62], L. Cunqueiro[37], J. Cussonneau[71], A. Dainese[79],
H.H. Dalsgaard[28], A. Danu[16], I. Das[52], A. Dash[11], S. Dash[11], G.O.V. de Barros[92], A. De Caro[89], G. de Cataldo[6],
J. de Cuveland[43,c], A. De Falco[19], A. De Gaspari[44], J. de Groot[40], D. De Gruttola[89], N. De Marco[104],
S. De Pasquale[89], R. De Remigis[104], R. de Rooij[105], G. de Vaux[22], H. Delagrange[71], Y. Delgado[58], G. Dellacasa[1],
A. Deloff[107], V. Demanov[93], E. Dénes[18], A. Deppman[92], G. D'Erasmo[5], D. Derkach[97], A. Devaux[26], D. Di Bari[5],
C. Di Giglio[5,k], S. Di Liberto[87], A. Di Mauro[40], P. Di Nezza[37], M. Dialinas[71], L. Díaz[62], R. Díaz[49], T. Dietel[70],
R. Divià[40], Ø. Djuvsland[8], V. Dobretsov[68], A. Dobrin[60], T. Dobrowolski[107], B. Dönigus[31], I. Domínguez[62],
D.M.M. Don[46], O. Dordic[77], A.K. Dubey[53], J. Dubuisson[40], L. Ducroux[106], P. Dupieux[26], A.K. Dutta Majumdar[52],
M.R. Dutta Majumdar[53], D. Elia[6], D. Emschermann[44,o], H. Engel[43], A. Enokizono[74], B. Espagnon[76], M. Estienne[71],
S. Esumi[102], D. Evans[12], S. Evrard[40], G. Eyyubova[77], C.W. Fabjan[40,p], D. Fabris[79], J. Faivre[41], D. Falchieri[13],
A. Fantoni[37], M. Fasel[31], O. Fateev[34], R. Fearick[22], A. Fedunov[34], D. Fehlker[8], V. Fekete[15], D. Felea[16],
B. Fenton-Olsen[28,q], G. Feofilov[97], A.Fernández Téllez[83], E.G. Ferreiro[91], A. Ferretti[103], R. Ferretti[1,r],
M.A.S. Figueredo[92], S. Filchagin[93], R. Fini[6], F.M. Fionda[5], E.M. Fiore[5], M. Floris[19,k], Z. Fodor[18], S. Foertsch[22],
P. Foka[31], S. Fokin[68], F. Formenti[40], E. Fragiacomo[101], M. Fragkiadakis[4], U. Frankenfeld[31], A. Frolov[73], U. Fuchs[40],
F. Furano[40], C. Furget[41], M. Fusco Girard[89], J.J. Gaardhøje[28], S. Gadrat[41], M. Gagliardi[103], A. Gago[58],
M. Gallio[103], P. Ganoti[4], M.S. Ganti[53], C. Garabatos[31], C. García Trapaga[103], J. Gebelein[43], R. Gemme[1],

M. Germain[71], A. Gheata[40], M. Gheata[40], B. Ghidini[5], P. Ghosh[53], G. Giraudo[104], P. Giubellino[104],
E. Gladysz-Dziadus[29], R. Glasow[70,t], P. Glässel[44], A. Glenn[59], R.Gómez Jiménez[30], H. González Santos[83],
L.H. González-Trueba[63], P. González-Zamora[61], S. Gorbunov[43,c], Y. Gorbunov[75], S. Gotovac[96], H. Gottschlag[70],
V. Grabski[63], R. Grajcarek[44], A. Grelli[105], A. Grigoras[40], C. Grigoras[40], V. Grigoriev[67], A. Grigoryan[112],
S. Grigoryan[34], B. Grinyov[50], N. Grion[101], P. Gros[60], J.F. Grosse-Oetringhaus[40], J.-Y. Grossiord[106], R. Grosso[79],
F. Guber[65], R. Guernane[41], C. Guerra[58], B. Guerzoni[13], K. Gulbrandsen[28], H. Gulkanyan[112], T. Gunji[99],
A. Gupta[48], R. Gupta[48], H.-A. Gustafsson[60,t], H. Gutbrod[31], Ø. Haaland[8], C. Hadjidakis[76], M. Haiduc[16],
H. Hamagaki[99], G. Hamar[18], J. Hamblen[51], B.H. Han[94], J.W. Harris[72], M. Hartig[36], A. Harutyunyan[112],
D. Hasch[37], D. Hasegan[16], D. Hatzifotiadou[14], A. Hayrapetyan[112], M. Heide[70], M. Heinz[72], H. Helstrup[9],
A. Herghelegiu[17], C. Hernández[31], G. Herrera Corral[64], N. Herrmann[44], K.F. Hetland[9], B. Hicks[72], A. Hiei[45],
P.T. Hille[77,u], B. Hippolyte[98], T. Horaguchi[45,v], Y. Hori[99], P. Hristov[40], I. Hřivnáčová[76], S. Hu[7], M. Huang[8],
S. Huber[31], T.J. Humanic[27], D. Hutter[35], D.S. Hwang[94], R. Ichou[71], R. Ilkaev[93], I. Ilkiv[107], M. Inaba[102],
P.G. Innocenti[40], M. Ippolitov[68], M. Irfan[2], C. Ivan[105], A. Ivanov[97], M. Ivanov[31], V. Ivanov[39], T. Iwasaki[45],
A. Jachołkowski[40], P. Jacobs[10], L. Jančurová[34], S. Jangal[98], R. Janik[15], C. Jena[11], S. Jena[69], L. Jirden[40],
G.T. Jones[12], P.G. Jones[12], P. Jovanović[12], H. Jung[38], W. Jung[38], A. Jusko[12], A.B. Kaidalov[66], S. Kalcher[43,c],
P. Kaliňák[56], M. Kalisky[70], T. Kalliokoski[49], A. Kalweit[32], A. Kamal[2], R. Kamermans[105], K. Kanaki[8], E. Kang[38],
J.H. Kang[95], J. Kapitan[85], V. Kaplin[67], S. Kapusta[40], O. Karavichev[65], T. Karavicheva[65], E. Karpechev[65],
A. Kazantsev[68], U. Kebschull[43], R. Keidel[110], M.M. Khan[2], S.A. Khan[53], A. Khanzadeev[39], Y. Kharlov[82],
D. Kikola[108], B. Kileng[9], D.J. Kim[49], D.S. Kim[38], D.W. Kim[38], H.N. Kim[38], J. Kim[82], J.H. Kim[94], J.S. Kim[38],
M. Kim[38], M. Kim[95], S.H. Kim[38], S. Kim[94], Y. Kim[95], S. Kirsch[40], I. Kisel[43,e], S. Kiselev[66], A. Kisiel[27,k], J.L. Klay[90],
J. Klein[44], C. Klein-Bösing[40,o], M. Kliemant[36], A. Klovning[8], A. Kluge[40], M.L. Knichel[31], S. Kniege[36], K. Koch[44],
R. Kolevatov[77], A. Kolojvari[97], V. Kondratiev[97], N. Kondratyeva[67], A. Konevskih[65], E. Kornaś[29], R. Kour[12],
M. Kowalski[29], S. Kox[41], K. Kozlov[68], J. Kral[80,l], I. Králik[56], F. Kramer[36], I. Kraus[32,e], A. Kravčáková[55],
T. Krawutschke[54], M. Krivda[12], D. Krumbhorn[44], M. Krus[80], E. Kryshen[39], M. Krzewicki[3], Y. Kucheriaev[68],
C. Kuhn[98], P.G. Kuijer[3], L. Kumar[25], N. Kumar[25], R. Kupczak[108], P. Kurashvili[107], A. Kurepin[65], A.N. Kurepin[65],
A. Kuryakin[93], S. Kushpil[85], V. Kushpil[85], M. Kutouski[34], H. Kvaerno[77], M.J. Kweon[44], Y. Kwon[95], P. La Rocca[23,w],
F. Lackner[40], P.Ladrón de Guevara[61], V. Lafage[76], C. Lal[48], C. Lara[43], D.T. Larsen[8], G. Laurenti[14], C. Lazzeroni[12],
Y. Le Bornec[76], N. Le Bris[71], H. Lee[84], K.S. Lee[38], S.C. Lee[38], F. Lefèvre[71], M. Lenhardt[71], L. Leistam[40],
J. Lehnert[36], V. Lenti[6], H. León[63], I.León Monzón[30], H.León Vargas[36], P. Lévai[18], X. Li[7], Y. Li[7], R. Lietava[12],
S. Lindal[77], V. Lindenstruth[43,c], C. Lippmann[40], M.A. Lisa[27], L. Liu[8], V. Loginov[67], S. Lohn[40], X. Lopez[26],
M. López Noriega[76], R. López-Ramírez[83], E. López Torres[42], G. Løvhøiden[77], A. Lozea Feijo Soares[92], S. Lu[7],
M. Lunardon[78], G. Luparello[103], L. Luquin[71], J.-R. Lutz[98], K. Ma[111], R. Ma[72], D.M. Madagodahettige-Don[46],
A. Maevskaya[65], M. Mager[32,k], D.P. Mahapatra[11], A. Maire[98], I. Makhlyueva[40], D. Mal'Kevich[66], M. Malaev[39],
K.J. Malagalage[75], I. Maldonado Cervantes[62], M. Malek[76], T. Malkiewicz[49], P. Malzacher[31], A. Mamonov[93],
L. Manceau[26], L. Mangotra[48], V. Manko[68], F. Manso[26], V. Manzari[6], Y. Mao[111,y], J. Mareš[81], G.V. Margagliotti[100],
A. Margotti[14], A. Marín[31], I. Martashvili[51], P. Martinengo[40], M.I. Martínez Hernández[83], A. Martínez Davalos[63],
G. Martínez García[71], Y. Maruyama[45], A. Marzari Chiesa[103], S. Masciocchi[31], M. Masera[103], M. Masetti[13],
A. Masoni[20], L. Massacrier[106], M. Mastromarco[6], A. Mastroserio[5,k], Z.L. Matthews[12], A. Matyja[29,ai], D. Mayani[62],
G. Mazza[104], M.A. Mazzoni[87], F. Meddi[86], A. Menchaca-Rocha[63], P. Mendez Lorenzo[40], M. Meoni[40],
J. Mercado Pérez[44], P. Mereu[104], Y. Miake[102], A. Michalon[98], N. Miftakhov[39], L. Milano[103], J. Milosevic[77],
F. Minafra[5], A. Mischke[105], D. Miśkowiec[31], C. Mitu[16], K. Mizoguchi[45], J. Mlynarz[33], B. Mohanty[53], L. Molnar[18,k],
M.M. Mondal[53], L. Montaño Zetina[64,z], M. Monteno[104], E. Montes[61], M. Morando[78], S. Moretto[78], A. Morsch[40],
T. Moukhanova[68], V. Muccifora[37], E. Mudnic[96], S. Muhuri[53], H. Müller[40], M.G. Munhoz[92], J. Munoz[83], L. Musa[40],
A. Musso[104], B.K. Nandi[69], R. Nania[14], E. Nappi[6], F. Navach[5], S. Navin[12], T.K. Nayak[53], S. Nazarenko[93],
G. Nazarov[93], A. Nedosekin[66], F. Nendaz[106], J. Newby[59], A. Nianine[68], M. Nicassio[6,k], B.S. Nielsen[28], S. Nikolaev[68],
V. Nikolic[113], S. Nikulin[68], V. Nikulin[39], B.S. Nilsen[75], M.S. Nilsson[77], F. Noferini[14], P. Nomokonov[34], G. Nooren[105],
N. Novitzky[49], A. Nyatha[69], C. Nygaard[28], A. Nyiri[77], J. Nystrand[8], A. Ochirov[97], G. Odyniec[10], H. Oeschler[32,a],
M. Oinonen[49], K. Okada[99], Y. Okada[45], M. Oldenburg[40], J. Oleniacz[108], C. Oppedisano[104], F. Orsini[88], A. Ortiz
Velasquez[62], G. Ortona[103], A. Oskarsson[60], F. Osmic[40], L. Österman[60], P. Ostrowski[108], I. Otterlund[60],
J. Otwinowski[31], G. Øvrebekk[8], K. Oyama[44], K. Ozawa[99], Y. Pachmayer[44], M. Pachr[80], F. Padilla[103], P. Pagano[89],
G. Paić[62], F. Painke[43], C. Pajares[91], S. Pal[52,ab], S.K. Pal[53], A. Palaha[12], A. Palmeri[24], R. Panse[43], V. Papikyan[112],
G.S. Pappalardo[24], W.J. Park[31], B. Pastirčák[56], C. Pastore[6], V. Paticchio[6], A. Pavlinov[33], T. Pawlak[108],

T. Peitzmann[105], A. Pepato[79], H. Pereira[88], D. Peressounko[68], C. Pérez[58], D. Perini[40], D. Perrino[5,k], W. Peryt[108], J. Peschek[43,c], A. Pesci[14], V. Peskov[62,k], Y. Pestov[73], A.J. Peters[40], V. Petráček[80], A. Petridis[4,t], M. Petris[17], P. Petrov[12], M. Petrovici[17], C. Petta[23], J. Peyré[76], S. Piano[101], A. Piccotti[104], M. Pikna[15], P. Pillot[71], O. Pinazza[14,k], L. Pinsky[46], N. Pitz[36], F. Piuz[40], R. Platt[12], M. Płoskoń[10], J. Pluta[108], T. Pocheptsov[34,ac], S. Pochybova[18], P.L.M. Podesta Lerma[30], F. Poggio[103], M.G. Poghosyan[103], K. Polák[81], B. Polichtchouk[82], P. Polozov[66], V. Polyakov[39], B. Pommeresch[8], A. Pop[17], F. Posa[5], V. Pospíšil[80], B. Potukuchi[48], J. Pouthas[76], S.K. Prasad[53], R. Preghenella[13,w], F. Prino[104], C.A. Pruneau[33], I. Pshenichnov[65], G. Puddu[19], P. Pujahari[69], A. Pulvirenti[23], A. Punin[93], V. Punin[93], M. Putiš[55], J. Putschke[72], E. Quercigh[40], A. Rachevski[101], A. Rademakers[40], S. Radomski[44], T.S. Räihä[49], J. Rak[49], A. Rakotozafindrabe[88], L. Ramello[1], A. Ramírez Reyes[64], M. Rammler[70], R. Raniwala[47], S. Raniwala[47], S.S. Räsänen[49], I. Rashevskaya[101], S. Rath[11], K.F. Read[51], J.S. Real[41], K. Redlich[107,ap], R. Renfordt[36], A.R. Reolon[37], A. Reshetin[65], F. Rettig[43,c], J.-P. Revol[40], K. Reygers[70,ad], H. Ricaud[32], L. Riccati[104], R.A. Ricci[57], M. Richter[8], P. Riedler[40], W. Riegler[40], F. Riggi[23], A. Rivetti[104], M.Rodriguez Cahuantzi[83], K. Røed[9], D. Röhrich[40,af], S.Román López[83], R. Romita[5,e], F. Ronchetti[37], P. Rosinský[40], P. Rosnet[26], S. Rossegger[40], A. Rossi[100,aq], F. Roukoutakis[40,ag], S. Rousseau[76], C. Roy[71,m], P. Roy[52], A.J. Rubio-Montero[61], R. Rui[100], I. Rusanov[44], G. Russo[89], E. Ryabinkin[68], A. Rybicki[29], S. Sadovsky[82], K. Šafařík[40], R. Sahoo[78], J. Saini[53], P. Saiz[40], D. Sakata[102], C.A. Salgado[91], R. Salgueiro Domingues da Silva[40], S. Salur[10], T. Samanta[53], S. Sambyal[48], V. Samsonov[39], L. Šándor[56], A. Sandoval[63], M. Sano[102], S. Sano[99], R. Santo[70], R. Santoro[5], J. Sarkamo[49], P. Saturnini[26], E. Scapparone[14], F. Scarlassara[78], R.P. Scharenberg[109], C. Schiaua[17], R. Schicker[44], H. Schindler[40], C. Schmidt[31], H.R. Schmidt[31], K. Schossmaier[40], S. Schreiner[40], S. Schuchmann[36], J. Schukraft[40], Y. Schutz[71], K. Schwarz[31], K. Schweda[44], G. Scioli[13], E. Scomparin[104], P.A. Scott[12], G. Segato[78], D. Semenov[97], S. Senyukov[1], J. Seo[38], S. Serci[19], L. Serkin[62], E. Serradilla[61], A. Sevcenco[16], I. Sgura[5], G. Shabratova[34], R. Shahoyan[40], G. Sharkov[66], N. Sharma[25], S. Sharma[48], K. Shigaki[45], M. Shimomura[102], K. Shtejer[42], Y. Sibiriak[68], M. Siciliano[103], E. Sicking[40,ah], E. Siddi[20], T. Siemiarczuk[107], A. Silenzi[13], D. Silvermyr[74], E. Simili[105], G. Simonetti[5,k], R. Singaraju[53], R. Singh[48], V. Singhal[53], B.C. Sinha[53], T. Sinha[52], B. Sitar[15], M. Sitta[1], T.B. Skaali[77], K. Skjerdal[8], R. Smakal[80], N. Smirnov[72], R. Snellings[3], H. Snow[12], C. Søgaard[28], A. Soloviev[82], H.K. Soltveit[44], R. Soltz[59], W. Sommer[36], C.W. Son[84], H. Son[94], M. Song[95], C. Soos[40], F. Soramel[78], D. Soyk[31], M. Spyropoulou-Stassinaki[4], B.K. Srivastava[109], J. Stachel[44], F. Staley[88], E. Stan[16], G. Stefanek[107], G. Stefanini[40], T. Steinbeck[43,c], E. Stenlund[60], G. Steyn[22], D. Stocco[103,ai], R. Stock[36], P. Stolpovsky[82], P. Strmen[15], A.A.P. Suaide[92], M.A. Subieta Vásquez[103], T. Sugitate[45], C. Suire[76], M. Šumbera[85], T. Susa[113], D. Swoboda[40], J. Symons[10], A. Szanto de Toledo[92], I. Szarka[15], A. Szostak[20], M. Szuba[108], M. Tadel[40], C. Tagridis[4], A. Takahara[99], J. Takahashi[21], R. Tanabe[102], J.D. Tapia Takaki[76], H. Taureg[40], A. Tauro[40], M. Tavlet[40], G. Tejeda Muñoz[83], A. Telesca[40], C. Terrevoli[5], J. Thäder[43,c], R. Tieulent[106], D. Tlusty[80], A. Toia[40], T. Tolyhy[18], C. Torcato de Matos[40], H. Torii[45], G. Torralba[43], L. Toscano[104], F. Tosello[104], A. Tournaire[71,aj], T. Traczyk[108], P. Tribedy[53], G. Tröger[43], D. Truesdale[27], W.H. Trzaska[49], G. Tsiledakis[44], E. Tsilis[4], T. Tsuji[99], A. Tumkin[93], R. Turrisi[79], A. Turvey[75], T.S. Tveter[77], H. Tydesjö[40], K. Tywoniuk[77], J. Ulery[36], K. Ullaland[8], A. Uras[19], J. Urbán[55], G.M. Urciuoli[87], G.L. Usai[19], A. Vacchi[101], M. Vala[34,j], L.Valencia Palomo[63], S. Vallero[44], N. van der Kolk[3], P.Vande Vyvre[40], M. van Leeuwen[105], L. Vannucci[57], A. Vargas[83], R. Varma[69], A. Vasiliev[68], I. Vassiliev[43,ag], M. Vasileiou[4], V. Vechernin[97], M. Venaruzzo[100], E. Vercellin[103], S. Vergara[83], R. Vernet[23,ak], M. Verweij[105], I. Vetlitskiy[66], L. Vickovic[96], G. Viesti[78], O. Vikhlyantsev[93], Z. Vilakazi[22], O. Villalobos Baillie[12], A. Vinogradov[68], L. Vinogradov[97], Y. Vinogradov[93], T. Virgili[89], Y.P. Viyogi[53], A. Vodopianov[34], K. Voloshin[66], S. Voloshin[33], G. Volpe[5], B. von Haller[40], D. Vranic[31], J. Vrláková[55], B. Vulpescu[26], B. Wagner[8], V. Wagner[80], L. Wallet[40], R. Wan[111,m], D. Wang[111], Y. Wang[44], Y. Wang[111], K. Watanabe[102], Q. Wen[7], J. Wessels[70], U. Westerhoff[70], J. Wiechula[44], J. Wikne[77], A. Wilk[70], G. Wilk[107], M.C.S. Williams[14], N. Willis[76], B. Windelband[44], C. Xu[111], C. Yang[111], H. Yang[44], S. Yasnopolskiy[68], F. Yermia[71], J. Yi[84], Z. Yin[111], H. Yokoyama[102], I.-K. Yoo[84], X. Yuan[111,am], V. Yurevich[34], I. Yushmanov[68], E. Zabrodin[77], B. Zagreev[66], A. Zalite[39], C. Zampolli[40,an], Y. Zanevsky[34], S. Zaporozhets[34], A. Zarochentsev[97], P. Závada[81], H. Zbroszczyk[108], P. Zelnicek[43], A. Zenin[82], A. Zepeda[64], I. Zgura[16], M. Zhalov[39], X. Zhang[111,b], D. Zhou[111], S. Zhou[7], J. Zhu[111], A. Zichichi[13,w], A. Zinchenko[34], G. Zinovjev[50], Y. Zoccarato[106], V. Zycháček[80], M. Zynovyev[50]

[1]Dipartimento di Scienze e Tecnologie Avanzate dell'Università del Piemonte Orientale and Gruppo Collegato INFN, Alessandria, Italy
[2]Department of Physics, Aligarh Muslim University, Aligarh, India
[3]Nikhef, National Institute for Subatomic Physics, Amsterdam, Netherlands
[4]Physics Department, University of Athens, Athens, Greece
[5]Dipartimento Interateneo di Fisica 'M. Merlin' and Sezione INFN, Bari, Italy

[6] Sezione INFN, Bari, Italy
[7] China Institute of Atomic Energy, Beijing, China
[8] Department of Physics and Technology, University of Bergen, Bergen, Norway
[9] Faculty of Engineering, Bergen University College, Bergen, Norway
[10] Lawrence Berkeley National Laboratory, Berkeley, CA, USA
[11] Institute of Physics, Bhubaneswar, India
[12] School of Physics and Astronomy, University of Birmingham, Birmingham, UK
[13] Dipartimento di Fisica dell'Università and Sezione INFN, Bologna, Italy
[14] Sezione INFN, Bologna, Italy
[15] Faculty of Mathematics, Physics and Informatics, Comenius University, Bratislava, Slovakia
[16] Institute of Space Sciences (ISS), Bucharest, Romania
[17] National Institute for Physics and Nuclear Engineering, Bucharest, Romania
[18] KFKI Research Institute for Particle and Nuclear Physics, Hungarian Academy of Sciences, Budapest, Hungary
[19] Dipartimento di Fisica dell'Università and Sezione INFN, Cagliari, Italy
[20] Sezione INFN, Cagliari, Italy
[21] Universidade Estadual de Campinas (UNICAMP), Campinas, Brazil
[22] Physics Department, University of Cape Town, iThemba Laboratories, Cape Town, South Africa
[23] Dipartimento di Fisica e Astronomia dell'Università and Sezione INFN, Catania, Italy
[24] Sezione INFN, Catania, Italy
[25] Physics Department, Panjab University, Chandigarh, India
[26] Laboratoire de Physique Corpusculaire (LPC), Clermont Université, Université Blaise Pascal, CNRS-IN2P3, Clermont-Ferrand, France
[27] Department of Physics, Ohio State University, Columbus, OH, USA
[28] Niels Bohr Institute, University of Copenhagen, Copenhagen, Denmark
[29] The Henryk Niewodniczanski Institute of Nuclear Physics, Polish Academy of Sciences, Cracow, Poland
[30] Universidad Autónoma de Sinaloa, Culiacán, Mexico
[31] Research Division and ExtreMe Matter Institute EMMI, GSI Helmholtzzentrum für Schwerionenforschung, Darmstadt, Germany
[32] Institut für Kernphysik, Technische Universität Darmstadt, Darmstadt, Germany
[33] Wayne State University, Detroit, MI, USA
[34] Joint Institute for Nuclear Research (JINR), Dubna, Russia
[35] Frankfurt Institute for Advanced Studies, Johann Wolfgang Goethe-Universität Frankfurt, Frankfurt, Germany
[36] Institut für Kernphysik, Johann Wolfgang Goethe-Universität Frankfurt, Frankfurt, Germany
[37] Laboratori Nazionali di Frascati, INFN, Frascati, Italy
[38] Gangneung-Wonju National University, Gangneung, South Korea
[39] Petersburg Nuclear Physics Institute, Gatchina, Russia
[40] European Organization for Nuclear Research (CERN), Geneva, Switzerland
[41] Laboratoire de Physique Subatomique et de Cosmologie (LPSC), Université Joseph Fourier, CNRS-IN2P3, Institut Polytechnique de Grenoble, Grenoble, France
[42] Centro de Aplicaciones Tecnológicas y Desarrollo Nuclear (CEADEN), Havana, Cuba
[43] Kirchhoff-Institut für Physik, Ruprecht-Karls-Universität Heidelberg, Heidelberg, Germany
[44] Physikalisches Institut, Ruprecht-Karls-Universität Heidelberg, Heidelberg, Germany
[45] Hiroshima University, Hiroshima, Japan
[46] University of Houston, Houston, TX, USA
[47] Physics Department, University of Rajasthan, Jaipur, India
[48] Physics Department, University of Jammu, Jammu, India
[49] Helsinki Institute of Physics (HIP) and University of Jyväskylä, Jyväskylä, Finland
[50] Bogolyubov Institute for Theoretical Physics, Kiev, Ukraine
[51] University of Tennessee, Knoxville, TN, USA
[52] Saha Institute of Nuclear Physics, Kolkata, India
[53] Variable Energy Cyclotron Centre, Kolkata, India
[54] Fachhochschule Köln, Köln, Germany
[55] Faculty of Science, P.J. Šafárik University, Košice, Slovakia
[56] Institute of Experimental Physics, Slovak Academy of Sciences, Košice, Slovakia
[57] Laboratori Nazionali di Legnaro, INFN, Legnaro, Italy
[58] Sección Física, Departamento de Ciencias, Pontificia Universidad Católica del Perú, Lima, Peru
[59] Lawrence Livermore National Laboratory, Livermore, CA, USA
[60] Division of Experimental High Energy Physics, University of Lund, Lund, Sweden
[61] Centro de Investigaciones Energéticas Medioambientales y Tecnológicas (CIEMAT), Madrid, Spain
[62] Instituto de Ciencias Nucleares, Universidad Nacional Autónoma de México, Mexico City, Mexico
[63] Instituto de Física, Universidad Nacional Autónoma de México, Mexico City, Mexico
[64] Centro de Investigación y de Estudios Avanzados (CINVESTAV), Mexico City and Mérida, Mexico
[65] Institute for Nuclear Research, Academy of Sciences, Moscow, Russia
[66] Institute for Theoretical and Experimental Physics, Moscow, Russia
[67] Moscow Engineering Physics Institute, Moscow, Russia
[68] Russian Research Centre Kurchatov Institute, Moscow, Russia
[69] Indian Institute of Technology, Mumbai, India
[70] Institut für Kernphysik, Westfälische Wilhelms-Universität Münster, Münster, Germany
[71] SUBATECH, Ecole des Mines de Nantes, Université de Nantes, CNRS-IN2P3, Nantes, France
[72] Yale University, New Haven, CT, USA
[73] Budker Institute for Nuclear Physics, Novosibirsk, Russia

[74]Oak Ridge National Laboratory, Oak Ridge, TN, USA

[75]Physics Department, Creighton University, Omaha, NE, USA

[76]Institut de Physique Nucléaire d'Orsay (IPNO), Université Paris-Sud, CNRS-IN2P3, Orsay, France

[77]Department of Physics, University of Oslo, Oslo, Norway

[78]Dipartimento di Fisica dell'Università and Sezione INFN, Padova, Italy

[79]Sezione INFN, Padova, Italy

[80]Faculty of Nuclear Sciences and Physical Engineering, Czech Technical University in Prague, Prague, Czech Republic

[81]Institute of Physics, Academy of Sciences of the Czech Republic, Prague, Czech Republic

[82]Institute for High Energy Physics, Protvino, Russia

[83]Benemérita Universidad Autónoma de Puebla, Puebla, Mexico

[84]Pusan National University, Pusan, South Korea

[85]Nuclear Physics Institute, Academy of Sciences of the Czech Republic, Řež u Prahy, Czech Republic

[86]Dipartimento di Fisica dell'Università 'La Sapienza' and Sezione INFN, Rome, Italy

[87]Sezione INFN, Rome, Italy

[88]Commissariat à l'Energie Atomique, IRFU, Saclay, France

[89]Dipartimento di Fisica 'E.R. Caianiello' dell'Università and Sezione INFN, Salerno, Italy

[90]California Polytechnic State University, San Luis Obispo, CA, USA

[91]Departamento de Física de Partículas and IGFAE, Universidad de Santiago de Compostela, Santiago de Compostela, Spain

[92]Universidade de São Paulo (USP), São Paulo, Brazil

[93]Russian Federal Nuclear Center (VNIIEF), Sarov, Russia

[94]Department of Physics, Sejong University, Seoul, South Korea

[95]Yonsei University, Seoul, South Korea

[96]Technical University of Split FESB, Split, Croatia

[97]V. Fock Institute for Physics, St. Petersburg State University, St. Petersburg, Russia

[98]Institut Pluridisciplinaire Hubert Curien (IPHC), Université de Strasbourg, CNRS-IN2P3, Strasbourg, France

[99]University of Tokyo, Tokyo, Japan

[100]Dipartimento di Fisica dell'Università and Sezione INFN, Trieste, Italy

[101]Sezione INFN, Trieste, Italy

[102]University of Tsukuba, Tsukuba, Japan

[103]Dipartimento di Fisica Sperimentale dell'Università and Sezione INFN, Turin, Italy

[104]Sezione INFN, Turin, Italy

[105]Nikhef and Institute for Subatomic Physics of Utrecht University, Utrecht, Netherlands

[106]Université de Lyon, Université Lyon 1, CNRS/IN2P3, IPN-Lyon, Villeurbanne, France

[107]Soltan Institute for Nuclear Studies, Warsaw, Poland

[108]Warsaw University of Technology, Warsaw, Poland

[109]Purdue University, West Lafayette, IN, USA

[110]Zentrum für Technologietransfer und Telekommunikation (ZTT), Fachhochschule Worms, Worms, Germany

[111]Hua-Zhong Normal University, Wuhan, China

[112]Yerevan Physics Institute, Yerevan, Armenia

[113]Rudjer Bošković Institute, Zagreb, Croatia

[a] e-mail: h.oeschler@gsi.de

[b] Also at Laboratoire de Physique Corpusculaire (LPC), Clermont Université, Université Blaise Pascal, CNRS-IN2P3, Clermont-Ferrand, France.

[c] Also at Frankfurt Institute for Advanced Studies, Johann Wolfgang Goethe-Universität Frankfurt, Frankfurt, Germany.

[d] Now at Sezione INFN, Padova, Italy.

[e] Now at Research Division and ExtreMe Matter Institute EMMI, GSI Helmholtzzentrum für Schwerionenforschung, Darmstadt, Germany.

[f] Now at Institut für Kernphysik, Johann Wolfgang Goethe-Universität Frankfurt, Frankfurt, Germany.

[g] Now at Physics Department, University of Cape Town, iThemba Laboratories, Cape Town, South Africa.

[h] Now at National Institute for Physics and Nuclear Engineering, Bucharest, Romania.

[i] Also at University of Houston, Houston, TX, United States.

[j] Now at Faculty of Science, P.J. Šafárik University, Košice, Slovakia.

[k] Now at European Organization for Nuclear Research (CERN), Geneva, Switzerland.

[l] Now at Helsinki Institute of Physics (HIP) and University of Jyväskylä, Jyväskylä, Finland.

[m] Now at Institut Pluridisciplinaire Hubert Curien (IPHC), Université de Strasbourg, CNRS-IN2P3, Strasbourg, France.

[n] Now at Sezione INFN, Bari, Italy.

[o] Now at Institut für Kernphysik, Westfälische Wilhelms-Universität Münster, Münster, Germany.

[p] Now at: University of Technology and Austrian Academy of Sciences, Vienna, Austria.

[q] Also at Lawrence Livermore National Laboratory, Livermore, CA, United States.

[r] Also at European Organization for Nuclear Research (CERN), Geneva, Switzerland.

[s] Now at Sección Física, Departamento de Ciencias, Pontificia Universidad Católica del Perú, Lima, Peru.

Abstract The production of π^+, π^-, K^+, K^-, p, and $\bar{p}$ at mid-rapidity has been measured in proton-proton collisions at $\sqrt{s} = 900$ GeV with the ALICE detector. Particle identification is performed using the specific energy loss in the inner tracking silicon detector and the time projection chamber. In addition, time-of-flight information is used to identify hadrons at higher momenta. Finally, the distinctive kink topology of the weak decay of charged kaons is used for an alternative measurement of the kaon transverse momentum (p_t) spectra. Since these various particle identification tools give the best separation capabilities over different momentum ranges, the results are combined to extract spectra from $p_t = 100$ MeV/c to 2.5 GeV/c. The measured spectra are further compared with QCD-inspired models which yield a poor description. The total yields and the mean p_t are compared with previous measurements, and the trends as a function of collision energy are discussed.

[t]Deceased.

[u]Now at Yale University, New Haven, CT, United States.

[v]Now at University of Tsukuba, Tsukuba, Japan.

[w]Also at Centro Fermi – Centro Studi e Ricerche e Museo Storico della Fisica "Enrico Fermi", Rome, Italy.

[x]Now at Dipartimento Interateneo di Fisica 'M. Merlin' and Sezione INFN, Bari, Italy.

[y]Also at Laboratoire de Physique Subatomique et de Cosmologie (LPSC), Université Joseph Fourier, CNRS-IN2P3, Institut Polytechnique de Grenoble, Grenoble, France.

[z]Now at Dipartimento di Fisica Sperimentale dell'Università and Sezione INFN, Turin, Italy.

[aa]Now at Physics Department, Creighton University, Omaha, NE, United States.

[ab]Now at Commissariat à l'Energie Atomique, IRFU, Saclay, France.

[ac]Also at Department of Physics, University of Oslo, Oslo, Norway.

[ad]Now at Physikalisches Institut, Ruprecht-Karls-Universität Heidelberg, Heidelberg, Germany.

[ae]Now at Institut für Kernphysik, Technische Universität Darmstadt, Darmstadt, Germany.

[af]Now at Department of Physics and Technology, University of Bergen, Bergen, Norway.

[ag]Now at Physics Department, University of Athens, Athens, Greece.

[ah]Also at Institut für Kernphysik, Westfälische Wilhelms-Universität Münster, Münster, Germany.

[ai]Now at SUBATECH, Ecole des Mines de Nantes, Université de Nantes, CNRS-IN2P3, Nantes, France.

[aj]Now at Université de Lyon, Université Lyon 1, CNRS/IN2P3, IPN-Lyon, Villeurbanne, France.

[ak]Now at: Centre de Calcul IN2P3, Lyon, France.

[al]Now at Variable Energy Cyclotron Centre, Kolkata, India.

[am]Also at Dipartimento di Fisica dell'Università and Sezione INFN, Padova, Italy.

[an]Also at Sezione INFN, Bologna, Italy.

[ao]Also at Dipartimento di Fisica dell´Università, Udine, Italy.

[ap]Also at Wrocław University, Wrocław, Poland.

[aq]Now at Dipartimento di Fisica dell'Università and Sezione INFN, Padova, Italy.

1 Introduction

In pp collisions at ultra-relativistic energies the bulk of the particles produced at mid-rapidity have transverse momenta, p_t, below 1 GeV/c. Their production is not calculable from first principles via perturbative Quantum Chromodynamics, and is not well modelled at lower collision energies. This low p_t particle production, and species composition, must therefore be measured, providing crucial input for the modelling of hadronic interactions and the hadronization process. It is important to study the bulk production of particles as a function of both p_t and particle species. With the advent of pp collisions at the Large Hadron Collider (LHC) at CERN a new energy regime is being explored, where particle production from hard interactions which are predominantly gluonic in nature, is expected to play an increasing role. Such data will provide extra constraints on the modelling of fragmentation functions. The data will also serve as a reference for the heavy-ion measurements.

The ALICE detector [1, 2] is designed to perform measurements in the high-multiplicity environment expected in central lead-lead collisions at $\sqrt{s_{NN}} = 5.5$ TeV at the LHC and to identify particles over a wide range of momenta. As such, it is ideally suited to perform these measurements also in pp collisions.

This paper presents the transverse momentum spectra and yields of identified particles at mid-rapidity from the first pp collisions collected in the autumn of 2009, during the commissioning of the LHC, at $\sqrt{s} = 900$ GeV. The evolution of particle production in pp collisions with collision energy is studied by comparing to data from previous experiments.

We report π^+, π^-, K^+, K^-, p, and $\bar{p}$ distributions, identified via several independent techniques utilizing specific energy loss, dE/dx, information from the Inner Tracking System (ITS) and the Time Projection Chamber (TPC), and velocity measurements in the Time-Of-Flight array (TOF). The combination of these methods provides particle identification over the transverse momentum range 0.1 GeV/c < p_t < 2.5 GeV/c. Charged kaons, identified via kink topology of their weak decays in the TPC, provide a complementary measurement over a similar p_t range. All reported particle yields are for primary particles, namely those directly produced in the collision including the products of strong and electromagnetic decays but excluding weak decays of strange particles.

The paper is organized as follows: In Sect. 2, the ALICE detectors relevant for these studies, the experimental conditions, and the corresponding analysis techniques are described. Details of the event and particle selection are presented. In Sect. 3, the π^+, π^-, K^+, K^-, p, and $\bar{p}$ inclusive spectra and yields, obtained by combining the various techniques described in Sect. 2, are presented. The results are compared with calculations from QCD-inspired models and

the p_t-dependence of ratios of particle yields, e.g. K/π and p/π, are discussed. Comparisons with data from other experiments at different $\sqrt{s}$ are made and the evolution of the ratio of strange to non-strange hadrons with collision energy is discussed. Finally, in Sect. 4 the results are summarized.

2 Experimental setup and data analysis

2.1 The ALICE detector

The ALICE detector and its expected performance are described in detail in [1–3]. For the analyses described in this paper the following detectors are used: the ITS, the TPC and the TOF detector. These detectors are positioned in a solenoidal magnetic field of $B = 0.5$ T and have a common pseudo-rapidity coverage of $-0.9 < \eta < 0.9$. Two forward scintillator hodoscopes (VZERO) are used for triggering purposes. They are placed on either side of the interaction region, covering regions $2.8 < \eta < 5.1$ and $-3.7 < \eta < -1.7$.

2.1.1 The Inner Tracking System

The ITS is the closest of the central barrel detectors to the beam axis. It is composed of six cylindrical layers of silicon detectors. The two innermost layers are equipped with pixel detectors (SPD), followed by two layers of drift detectors (SDD) and two layers of double-sided silicon strip detectors (SSD). The innermost layer is at 3.9 cm from the beam axis, while the outer layer is at 43.0 cm.

The ITS provides high-resolution space points that allow the extension of tracks reconstructed in the TPC towards the interaction vertex, thus improving momentum and angular resolution. The four layers equipped with SDD and SSD also provide a measurement of the specific energy loss dE/dx. The SPD yields an on-line measure of the multiplicity by counting the number of chips that have one or more hits (fast-OR), which is included in the minimum-bias trigger logic [3, 4]. The ITS is also used as a stand-alone tracker to reconstruct charged particles with momenta below 200 MeV/c that are deflected or decay before reaching the TPC, and to recover tracks crossing dead regions of the TPC. A detailed description of the three sub-systems can be found in [3]. The dE/dx measurement in the SDD and SSD has been calibrated using cosmic ray data and pp events [5]. The 2198 ITS modules have been aligned using survey information, cosmic-ray tracks and pp data with the methods described in [6]. The fraction of active modules per layer in the present setup is around 80% in the SPD and 90%–95% both in SDD and SSD.

2.1.2 The Time Projection Chamber

The TPC is the main tracking device. It is a large volume, high granularity, cylindrical detector with an outer radius of 2.78 m and a length of 5.1 m. The active volume extends from 0.85 m to 2.47 m in radius. It covers 2π in azimuth and $|\eta| < 0.9$ in polar angle for the full radial track length. Accepting one third of the full radial track length extends the range to $|\eta| < 1.5$. The 90 m^3 drift volume is filled with a Ne (85.7%), CO$_2$ (9.5%), and N$_2$ (4.8%) gas mixture. A high voltage central membrane splits the drift region in two halves, resulting in a maximal drift time of 94 µs. Each of the two read-out planes is composed of 18 inner and 18 outer chambers with a total of 159 pad rows, resulting in a total of 557 568 pads which are read out separately. The position resolution in $r\phi$ direction varies from 1100 µm to 800 µm when going from the inner to the outer radius. Along the beam axis (z, also the drift direction) the resolution ranges between 1250 µm and 1100 µm. A maximum of 159 clusters can be measured along a track in the TPC. For a detailed description see [7].

2.1.3 The Time-Of-Flight Detector

The TOF detector consists of 18 azimuthal sectors, each containing 91 Multi-gap Resistive Plate Chambers (MRPCs) distributed in five gas-tight modules. It is positioned at 370-399 cm from the beam axis. The region $260° < \phi < 320°$ at $\eta \sim 0$ is not covered in order to minimize the material in front of the Photon Spectrometer, which is not used in this analysis. The MRPC detectors are installed with a projective geometry along the beam direction, minimizing the variation of the flight path of particles across the sensitive area of the detector. Each MRPC is segmented into 96 read-out pads (2.5×3.5 cm^2 size), resulting in a total of 152928 channels. Test beam results demonstrated that the intrinsic time resolution of the detector is better than 50 ps, dominated by electronic effects and the time resolution of the time-to-digital converters [8]. Results from the TOF commissioning with cosmic rays are described in references [9–11]. In the present setup, 9.6% of the readout channels were inactive due to failures in the high- or low-voltage systems or in the readout electronics. The fraction of noisy channels, identified during data taking by online monitoring and excluded from the subsequent reconstruction, was below 0.1%.

2.2 Event selection and normalization

The data presented in this paper were collected during the commissioning of the LHC at CERN in the autumn of 2009, with pp collisions at $\sqrt{s} = 900$ GeV. The collider was run with four bunches per beam, resulting in two bunch crossings per beam circulation period (89 µs) at the ALICE interaction point. The remaining two bunches per beam were not

collided at ALICE, and served to estimate the contribution of beam-gas interactions. The average event rate was a few Hz, so the fraction of pile-up events was negligible.

The analysis is based on a sample of $\sim$300k inelastic pp collisions. The online trigger selection requires a signal in either of the VZERO counters or at least one hit in either of the SPD layers. The selection was improved offline with recomputed trigger input quantities using the time average over all VZERO hits and a suppression of noisy channels. The contamination from beam-induced background is rejected offline using the timing information of the VZERO and by cutting on the correlation between the number of clusters and track segments (tracklets) in the SPD detector [12, 13]. Selected events are further required to contain a reconstructed primary vertex. The vertex reconstruction efficiency calculated via Monte-Carlo simulations is 96.5% for events with one reconstructed track and approaches unity for events with more than two tracks.

The results presented in this paper are normalized to inelastic pp collisions, employing the strategy described in [12, 13]. In order to reduce the extrapolation and thus the systematic uncertainty on the normalization, the sample of selected events used for normalization includes triggered events without reconstructed tracks or vertices. Those events still contain a small contamination from very low multiplicity beam-induced background or accidentals from the trigger, which are not rejected by the selections described above. This contamination is of the order of 4% and is subtracted using the control triggers. From the analysis of empty bunch events the random contribution from cosmic rays is found to be negligible. The number of selected events is then converted to the number of inelastic collisions after correcting for the trigger efficiency, which is determined from the Monte-Carlo simulation, scaling the cross section for diffractive processes to the measurements of UA5 [14]. The subtraction of beam-gas events and the efficiency correction partially compensate each other: the overall correction factor is about 5% with a systematic uncertainty of about 2%, coming mainly from the uncertainties in the modelling of diffraction in the event generators.

In order to compare to previous experimental results, which are only published for the non-single-diffractive (NSD) class, in Sect. 3, we scale our spectra for the measured ratio $dN_{ch}/d\eta|_{NSD}/dN_{ch}/d\eta|_{INEL} \simeq 1.185$ [12]. PYTHIA and PHOJET simulations indicate that the p_t-dependence of the ratio of spectra for NSD and inelastic collisions is less than 5% in the reported range. Particle ratios are found to be insensitive to the conversion from inelastic to non-single-diffractive events.

2.3 Track selection

The identified particle spectra were measured independently with the ITS, TPC and TOF, and combined in the final stage

of the analysis. The rapidity range $|y| < 0.5$ was used for all analyses except for the kink analysis ($|y| < 0.7$).

For the TPC and TOF analyses, tracks reconstructed in the TPC are used. The TPC has full acceptance for tracks with $|\eta| < 0.9$. However, shorter tracks at higher η can still be used for physics analysis, in particular protons with a transverse momentum of $p_t = 400$ MeV/c and $|y| = 0.5$ which correspond to $|\eta| = 1.1$. To ensure high tracking efficiency and dE/dx-resolution, while keeping the contamination from secondaries and fakes low, tracks are required to have at least 80 clusters, and a χ^2 of the momentum fit that is smaller than 4 per cluster. Since each cluster in the TPC provides two degrees of freedom and the number of parameters of the track fit is much smaller than the number of clusters, the χ^2 cut is approximately 2 per degree of freedom. In addition, at least two clusters in the ITS must be associated to the track, out of which at least one is from the SPD. Tracks are further rejected based on their distance-of-closest approach (DCA) to the reconstructed event vertex. The cut is implemented as a function of p_t to correspond to about seven (five) standard deviations in the transverse (longitudinal) coordinate, taking into account the p_t-dependence of the impact parameter resolution. These selection criteria are tuned to select primary charged particles with high efficiency while minimizing the contributions from weak decays, conversions and secondary hadronic interactions in the detector material. The DCA resolution in the data is found to be in good agreement with the Monte-Carlo simulations that are used for efficiency corrections (see next Section).

Tracks reconstructed in the TPC are extrapolated to the sensitive layer of the TOF and a corresponding signal is searched for. The channel with the center closest to the track extrapolation point is selected if the distance is less than 10 cm. This rather weak criterion results in a high matching efficiency while keeping the fraction of wrongly associated tracks below 1% in the low-density environment presented by pp collisions.

The dE/dx measurements in the ITS are used to identify hadrons in two independent analyses, based on different tracking algorithms. One analysis uses the ITS-TPC combined tracking, while the other is based on ITS stand-alone tracks. The combined ITS-TPC tracking result serves as a cross-check of both the ITS stand-alone and the TPC results in the overlap region. The ITS stand-alone analysis extends the acceptance to lower p_t than the TPC or ITS-TPC analyses.

The combined ITS-TPC analysis uses the same track selection criteria as the TPC only analysis, with the additional requirement of at least four clusters in the ITS, out of which at least one must be in the SPD and at least three in SSD+SDD. This further reduces the contamination of secondaries and provides high resolution on track impact parameter and optimal resolution on the dE/dx. The ITS

stand-alone tracking uses a similar selection, with a different χ^2 selection and a different DCA selection. In the current tracking algorithm, ITS clusters are assigned a larger position error to account for residual misalignment of the detector. As a result, the χ^2 values are not properly normalized, but the selection was adjusted to be equivalent to the TPC χ^2 selection by inspecting the distributions. The DCA cut in the ITS analysis uses the same p_t-dependent parametrization as for TPC tracks, but with different parameters to account for the different resolution.

2.4 Monte-Carlo calculations

The efficiency and other correction factors including acceptance (jointly called *efficiency* in the following discussion) used in this paper are calculated from a Monte-Carlo simulation, based on over two million events produced with the PYTHIA 6.4 event generator [15] (tune D6T [16]), propagated through the detector with the GEANT3 [17] transport code. Dead and noisy channels as well as beam position and spread have been taken into account. A simulation based on the PHOJET event generator [18] is also used as a cross check.

GEANT3 is known to reproduce the absorption cross sections of hadrons incorrectly. The transport code FLU-KA contains a more accurate description of these cross sections [19–21], and a dedicated simulation is used to calculate a correction to the GEANT3 efficiency calculation [22]. This is relevant mainly for antiprotons at low p_t, where the correction is on the order of 10%. For other particles and at higher p_t, the difference between GEANT and FLUKA calculations is negligible.

2.5 Particle identification

The dE/dx and TOF signals are used for particle identification as a function of the momentum p, whereas the final spectra are given as a function of the transverse momentum p_t.

In the case of the TPC and ITS analyses, particles were identified via the specific energy loss dE/dx. Unique identification on a track-by-track basis is possible in regions of momentum where the bands are clearly separated from each other. In overlapping areas, particle identification is still possible on a statistical basis using fits to the energy loss distribution in each p_t-bin. The fits are performed on the distribution of the difference between the measured and the expected energy deposition for tracks within the selected rapidity range $|y| < 0.5$. This compensates for the very steep slope of the Bethe-Bloch in the $1/\beta^2$ region which would make the dE/dx-distribution in a simple p_t or p-slice non-Gaussian. The calculated expected energy loss depends on the measured track momentum p and the assumed mass for

the particle. The procedure is therefore repeated three times for the entire set of tracks, assuming the pion, kaon, and proton mass.

In the TPC analysis, the difference $[dE/dx]_{meas} - [dE/dx(\text{pid}, p_{tot})]_{calc}$ is used. For the ITS the difference of the logarithm of the measured and calculated energy deposit $\ln[dE/dx_{meas}] - \ln[dE/dx(\text{pid}, p_{tot})_{calc}]$ is taken to suppress the non-Gaussian tails originating from the smaller number of dE/dx measurements.

In the case of the TOF, the identification is based on the time-of-flight information. The procedure for the extraction of the raw yields differs slightly from the one used for TPC and ITS, and is described in Sect. 2.5.3.

2.5.1 Particle identification in the ITS

In both the ITS stand-alone and in the ITS-TPC analyses, the dE/dx measurement from the SDD and the SSD is used to identify particles. The stand-alone tracking result extends the momentum range to lower p_t than can be measured in the TPC, while the combined tracking provides a better momentum resolution.

The energy loss measurement in each layer of the ITS is corrected for the track length in the sensitive volume using tracking information. In the case of SDD clusters, a linear correction for the dependence of the reconstructed raw charge as a function of drift time due to the combined effect of charge diffusion and zero suppression is also applied [5]. For each track, dE/dx is calculated using a truncated mean: the average of the lowest two points in case four points are measured, or a weighted sum of the lowest (weight 1) and the second lowest point (weight 1/2), in case only three points are measured.

Figure 1 shows the truncated mean dE/dx for the sample of ITS stand-alone tracks along with the PHOBOS parametrization of the most probable value [23].
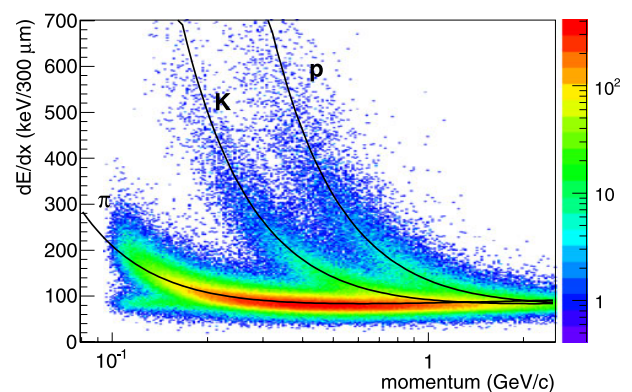
Fig. 1 (Color online) Specific energy loss dE/dx vs. momentum for tracks measured with the ITS. The solid lines are a parametrization (from [23]) of the detector response based on the Bethe–Bloch formula

For the ITS stand-alone track sample, the histograms are fitted with three Gaussians and the integral of the Gaussian centered at zero is used as the raw yield of the corresponding hadron species. In a first step, the peak widths σ of the peaks are extracted as a function of p_t for pions and protons in the region where their dE/dx distributions do not overlap with the kaon (and electron) distribution. For kaons, the same procedure is used at low p_t, where they are well separated. The p_t-dependence of the peak width is then extrapolated to higher p_t with the same functional form used to describe the pions and protons. The resulting parametrizations of the p_t dependence of σ are used to constrain the fits of the $\ln[dE/dx]$ distributions to extract the raw yields.

For the ITS-TPC combined track sample, a non-Gaussian tail is visible. This tail is a remnant of the tail of the Landau distribution for energy loss. It was verified using simulations that the shape and size of the tail are compatible with the expectations for a truncated mean using two out of four samples. The tail is not as pronounced for the ITS stand-alone track sample, due to the limited momentum resolution. The distribution is fitted with a combination of a Gaussian and an exponential function for the main peak and another exponential function to describe the tail of a background peak. This functional form provides an accurate description of the peak shape in the detector simulation, as well as the measured shape.

Examples of dE/dx distributions are shown in Fig. 2 for negative tracks using the kaon mass hypothesis in two different p_t intervals for both ITS stand-alone tracks (right panels) and ITS-TPC combined tracks (left panels).

Efficiency correction The raw hadron yields extracted from the fits to the dE/dx distributions are corrected for the reconstruction efficiency determined from Monte-Carlo simulations, applying the same analysis criteria to the simulated events as to the data. Secondary particles from interactions in the detector material and strange particle decays have been subtracted from the yield of both simulated and real data. The fraction of secondaries after applying the track impact-parameter cut depends on the hadron species and amounts to 1–3% for pions and 5–10% for protons depending on p_t. The secondary-to-primary ratio has been estimated by fitting the measured track impact-parameter distributions with three components, prompt particles, secondaries from strange particle decays and secondaries produced in the detector material for each hadron species. Al-
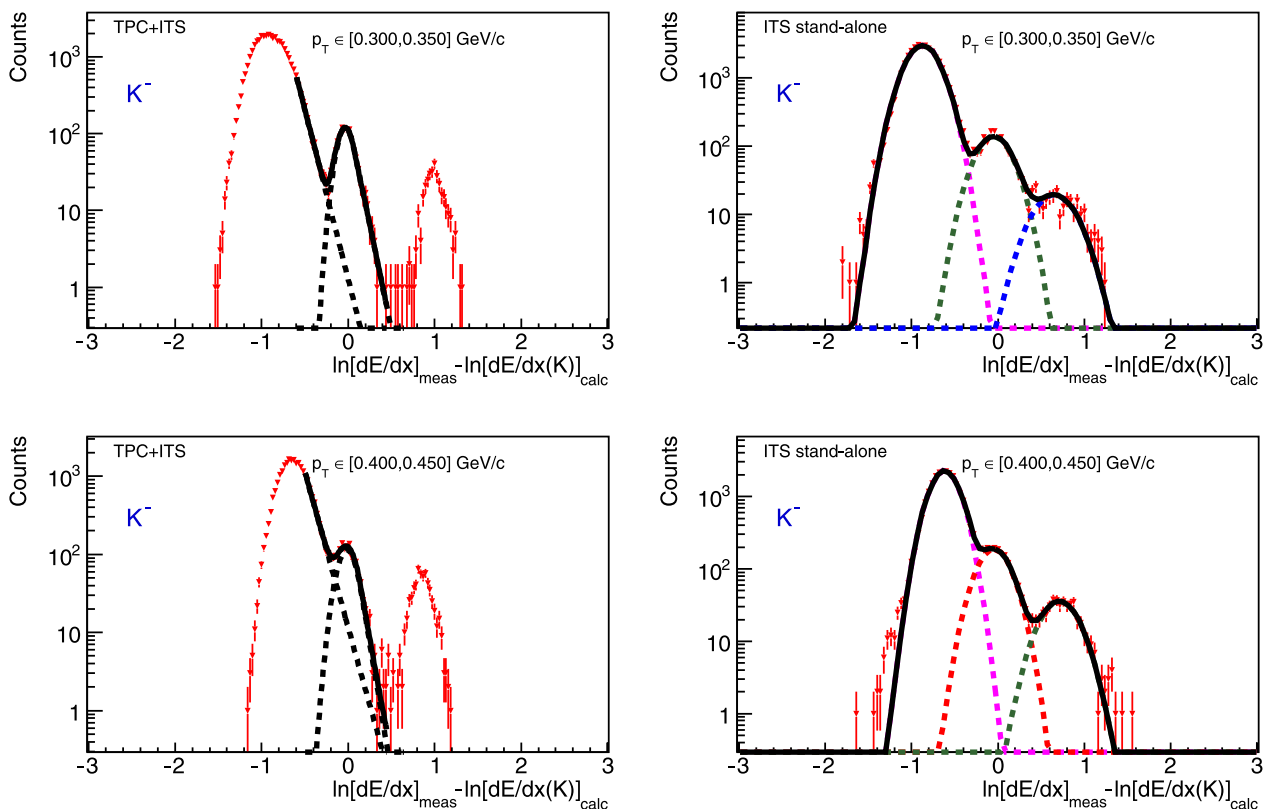
Fig. 2 (Color online) Distribution of $\ln[dE/dx]_{\text{meas}} - \ln[dE/dx(K)]_{\text{calc}}$ measured with the ITS in the two p_t-ranges, 300–350 MeV/c (*upper panels*) and 400–450 MeV/c (*lower panels*), using the kaon mass hypothesis. The *left panels* show the result for ITS-TPC combined tracks, while the *right panels* show the ITS stand-alone result. The *lines* indicate fits as described in the text

ternatively, the contamination from secondaries have been determined using Monte-Carlo samples, after rescaling the Λ yield to the measured values [24]. The difference between these two procedures is about 3% for protons and is negligible for other particles.

Figure 3 shows the total reconstruction efficiency for primary tracks in the ITS stand-alone, including the effects of detector and tracking efficiency, the track selection cuts and residual contamination in the fitting procedure, as determined from the Monte-Carlo simulation. This efficiency is used to correct the measured raw yields after subtraction of the contributions from secondary hadrons. The measured spectra are corrected for the efficiency of the primary vertex reconstruction with the SPD using the ratio between generated primary spectra in simulated events with a reconstructed vertex and events passing the trigger conditions.

Systematic errors are summarized in Table 1. The systematic uncertainty from secondary contamination has been estimated by repeating the full analysis chain with different cuts on the track impact parameter and by comparing the two alternative estimates outlined above. The effect of the uncertainty in the material budget has been estimated by modifying the material budget in the Monte-Carlo simulations by $\pm 7\%$, which is the present uncertainty of the ITS material budget. The systematic contribution from the fitting procedure to the $\ln[dE/dx]_{meas} - \ln[dE/dx(i)]_{calc}$ distributions has been estimated by varying the fit condition and by comparing to an independent analysis using a track-by-track identification approach based on the distance between

the measured and expected dE/dx values normalized to its resolution. The residual imperfections in the description of the ITS detector modules and dead areas in the simulation introduce another uncertainty in the ITS tracking efficiency. This is estimated by varying the cuts on the number of clusters and on the track χ^2 both in data and in Monte-Carlo simulations.

In the lowest p_t-bins, a larger systematic error has been assigned to account for the steep slope of the tracking efficiency as a function of the particle transverse momentum (see Fig. 3).

2.5.2 Particle identification in the TPC

Particle identification is based on the specific energy deposit of each particle in the drift gas of the TPC, shown in Fig. 4 as a function of momentum separately for positive and negative charges. The solid curves show the calibration curves obtained by fitting the ALEPH parametrization of the Bethe–Bloch curve [25] to the data points in regions of clear separation.

The calibration parameters have mostly been determined and tested via the analysis of cosmic rays. The pad-gain factors have been measured using the decay of radioactive $^{83}_{36}$Kr gas released into the TPC volume (for a detailed description see [7]).

As in the case of the ITS, a truncated-mean procedure is used to determine dE/dx (60% of the points are kept). This reduces the Landau tail of the dE/dx distribution to the extent that it is very close to a Gaussian distribution.

Examples of the dE/dx distribution in some p_t bins are shown in Fig. 5. The peak centered at zero is from kaons and the other peaks are from other particle species. As the background in all momentum bins is negligible, the integrals of the Gaussian give the raw yields.
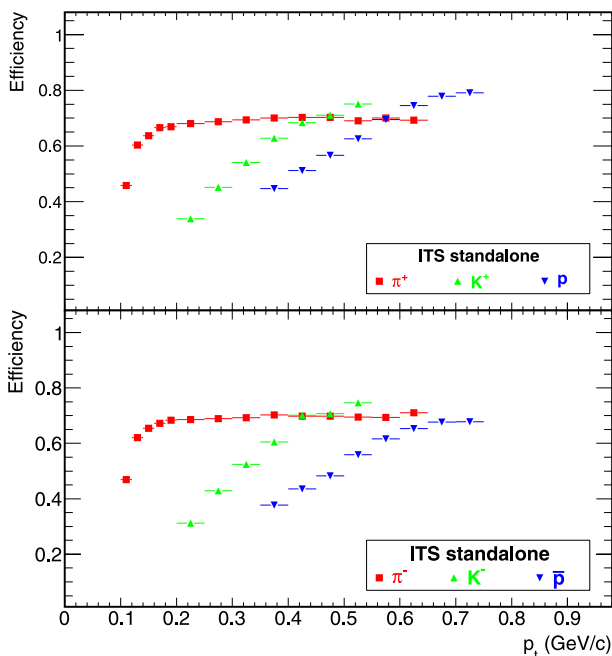
Fig. 3 (Color online) Efficiency for pions, kaons and protons for the ITS stand-alone analysis as obtained from Monte-Carlo simulations

Table 1 Summary of systematic errors in the efficiency correction of the ITS analysis

| Systematic errors	$\pi^{\pm}$	$K^{\pm}$	p and $\overline{p}$
Secondary contamination from material	negl.	negl.	negl.
Secondary contamination from weak decay	<1%	negl.	3%
Material budget			
highest p_t bin	<1%	<1%	1%
lowest p_t bin	5%	2%	3%
ITS efficiency			
all p_t bins	2%	2%	2%
lowest p_t bin	12%	13%	11%
$\ln(dE/dx)$ distr. fitting procedure	1%	5%	3.5%
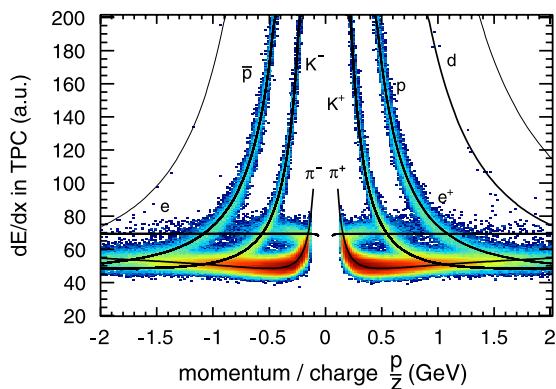
Fig. 4 (Color online) Specific energy loss dE/dx vs. momentum for tracks measured with the ALICE TPC. The *solid lines* are a parametrization of the Bethe–Bloch curve [25]

Efficiency correction The raw hadron spectra are corrected for the reconstruction efficiency, shown in Fig. 6, determined by doing the same analysis on Monte-Carlo events. The efficiency is calculated by comparing the number of reconstructed particles to the number of charged primary particles from PYTHIA in the chosen rapidity range. For transverse momenta above 800 MeV/c the efficiency saturates at roughly 80%. For kaons, the decay reduces the efficiency by about 30% at 250 MeV/c and 12% at 1.5 GeV/c. The range with a reconstruction efficiency lower than 60% (for pions and protons) is omitted for the analysis corresponding to a low-p_t cut-off of 200 MeV/c for pions, 250 MeV/c for kaons, and 400 MeV/c for protons.

Protons are corrected for the contamination of secondaries from material and of feed down from weak decays. The feed down was determined by two independent methods. Firstly, the contamination obtained from Monte-Carlo simulation was scaled such that it corresponds to the measured yield of Λs in the data [24]. Secondly, the shape of the impact parameter distribution was compared to the Monte-Carlo simulation. Weak decays produce a non-Gaussian tail in the distribution of primary particles whereas secondaries from material generate a flat background [22]. The remaining difference between the methods is included in the systematic error. The correction for weak decays amounts to up to 14% and the correction for secondaries from material up to 4% for protons with 400 MeV/c < p_t < 600 MeV/c. For other particle species and other transverse momenta the contamination is negligible.
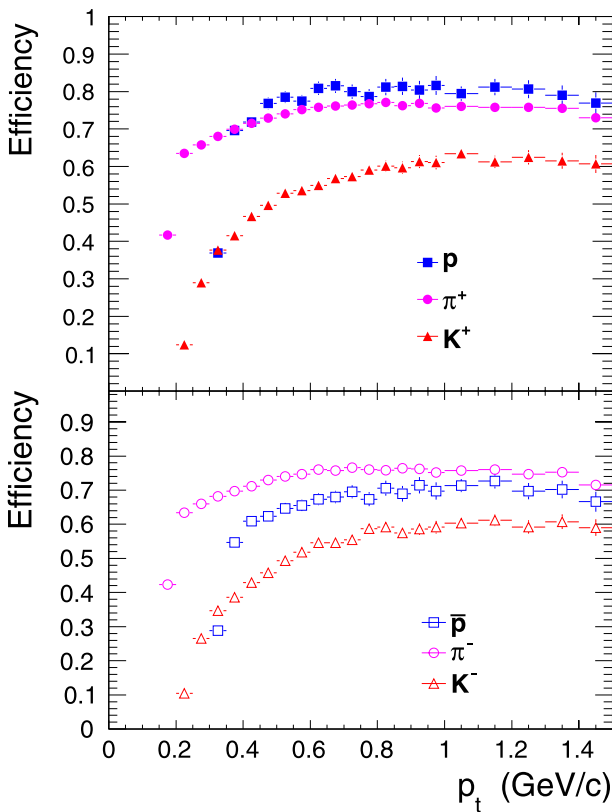
The systematic errors in the track reconstruction and in the removal of secondary particles have been estimated by varying the number of standard deviations in the distance-to-vertex cut, using a fixed cut of 3 cm instead of the variable one, and varying the SPD-TPC matching cut. Their impact on the corrected spectra is less than 5%. The influence of the uncertainty in the material budget has been examined by varying it by 7%. This resulted in the systematic errors
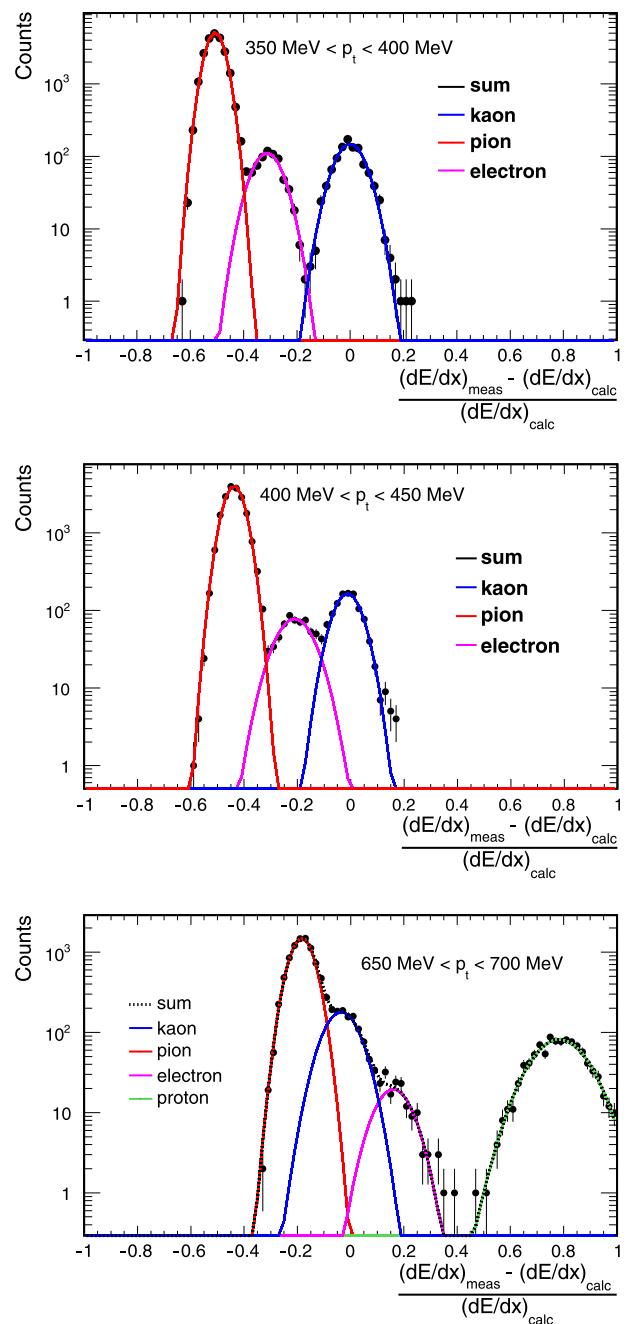
Fig. 5 (Color online) Distribution of $([dE/dx]_{meas}-[dE/dx(kaon)]_{calc})/[dE/dx(kaon)]_{calc}$ measured with the TPC for several p_t-bins showing the separation power. The *solid lines* are Gaussian fits to the distributions

given in Table 2. The uncertainty due to a possible deviation from a Gaussian shape has been established by comparing the multi-Gauss fit with a 3-σ band in well separated regions. The precision of the kink rejection is estimated to be within 3%.
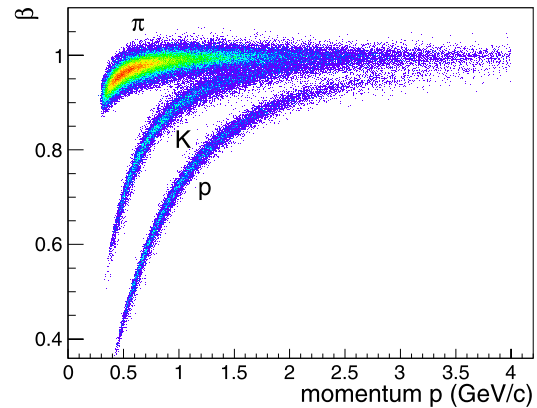
Fig. 6 (Color online) Efficiency of charged pions, kaons, and protons for the spectra extracted with the TPC

Fig. 7 (Color online) β of tracks of particles measured by TOF vs. their momentum

2.5.3 Particle identification with the TOF

Particles reaching the TOF system are identified by measuring their momentum and velocity simultaneously.

The velocity $\beta = L/t_{\text{TOF}}$ is obtained from the measured time of flight t_{TOF} and the reconstructed flight path L along the track trajectory between the point of closest approach to the event vertex and the TOF sensitive surface. The measured velocities are shown as a function of the momentum p at the vertex in Fig. 7. The bands corresponding to charged pions, kaons and protons are clearly visible. The width of the bands reflects the overall time-of-flight resolution of about 180 ps, which depends on the TOF timing signal resolution, the accuracy of the reconstructed flight path and the uncertainty of the event start time, t_0^{ev}. This last contribution is related to the uncertainty in establishing the absolute time of the collision. In the present sample this fluctuated with respect to the nominal time signal from the LHC with a σ of about 140 ps due to the finite size of the bunches.

To improve the overall time-of-flight resolution, the TOF information itself is used to determine t_0^{ev} in events having at least three tracks with an associated TOF signal. This is done with a combinatorial algorithm which compares the TOF times with the calculated times of the tracks for each event for different mass hypotheses. Using this procedure, the start-time has been improved for 44% of the tracks having an associated TOF signal and is rather independent on the momentum of the tracks. In this way the precision on the event start-time is about 85 ps on average.

Finally, tracks whose particle identity as determined from the TOF information is not compatible with the one inferred from the dE/dx signal in the TPC within five σ have been removed. This TOF-TPC compatibility criterion rejects about 0.6% of the tracks and further reduces the small contamination coming from tracks incorrectly associated with a TOF signal.

Table 2 Summary of systematic errors in the efficiency correction in the TPC analysis

Systematic errors	$\pi^{\pm}$	$K^{\pm}$	p and $\overline{\text{p}}$
Secondary contamination from material	negl.	negl.	<2%
Secondary contamination from weak decay	<4%	–	<10%
Energy loss and absorption in material	<1%	<1%	<2%
Kink rejection	negl.	<3%	–
Non-Gaussianity of dE/dx signal	negl.	negl.	negl.
Matching to ITS		<3%	

The correction for the event selection bias has been tested with two event generators, PYTHIA [15, 16] and PHOJET [18] and the corresponding uncertainty is less than 1%.

For each particle species i, the expected time of flight t^i_{calc} is calculated by summing up the time-of-flight increments $\Delta t_k = \Delta l_k \sqrt{p_k^2 + m_i^2}/p_k$ at each tracking step, with p_k being the local value of the track momentum, m_i the mass of the particle, and Δl_k the track-length increment along its trajectory. The yields of π, K and p are obtained from the simultaneous fit of the distribution of the time difference S between measured t_{TOF} and the average between the calculated time for pions and kaons

$$S = \left(t^\pi + t^K\right)_{\text{calc}}/2 - t_{\text{TOF}}. \qquad (1)$$

The symmetric treatment of kaons and pions in the definition of S ensures that the kaon and pion peak are both Gaussian. Extracting the yield for different species in a simultaneous fit guarantees that the resulting number of pions, kaons and protons matches the total number of tracks in the given momentum bin.

The distribution of the variable S is shown in Fig. 8 for three different transverse momentum bins for positive particles. The curves show the results of the three-Gaussian fit used to extract the raw yields. The integral of the fit result has been constrained to the number of entries in the distribution, and the means and the widths are allowed to vary within 5% and 10%, respectively, of their nominal values. The only free parameters in the fit are therefore the relative normalizations between the Gaussians.

The raw yields are extracted in different p_t-bins using a rapidity selection $|y_p| < 0.5$, where y_p is the rapidity calculated with the proton mass. For pions and kaons, this condition results in a larger y-acceptance and in both cases, the fraction outside of $|y| < 0.5$ has been subtracted in each p_t-bin taking into account the y-distribution of the yields within the pions and kaons peaks.

Efficiency correction Since the track selection used in the TOF analysis is the same as the one described in the TPC analysis (Sect. 2.5.2), the same tracking and feed-down corrections are applied. In the case of the TOF analysis, an additional correction is needed in order to take into account the fraction of the particles reconstructed by the TPC with an associated signal in TOF. This matching efficiency includes all sources of track losses in the propagation from the TPC to the TOF (geometry, decays and interactions with the material) and its matching with a TOF signal (the TOF intrinsic detector efficiency, the effect of dead channels and the efficiency of the track-TOF signal matching procedure). The TOF matching efficiency has been derived from Monte-Carlo events as the fraction of TPC reconstructed tracks having an associated TOF signal and is shown in Fig. 9 for each hadron species. The main factors limiting the TOF matching efficiency are the loss due to geometrical acceptance ($\approx 15\%$), the number of dead or noisy channels ($\approx 10\%$) and
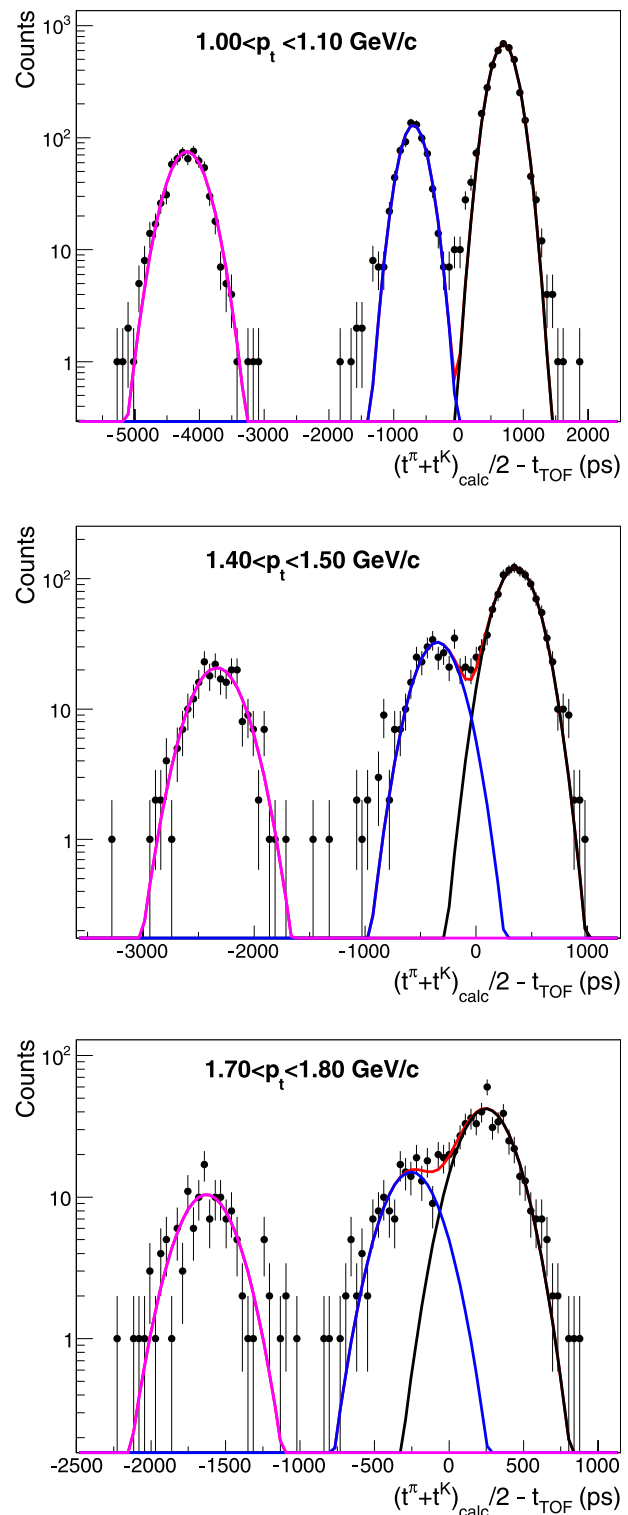
Fig. 8 (Color online) Distribution of the time difference between the measured TOF signal and the average of the calculated times for pions and kaons for several p_t-bins for positively charged particles. The fits are performed using Gaussian shapes

Fig. 9 (Color online) The TOF matching efficiency is shown for the three particles, separately, for (*top*) positive and (*bottom*) negative particles
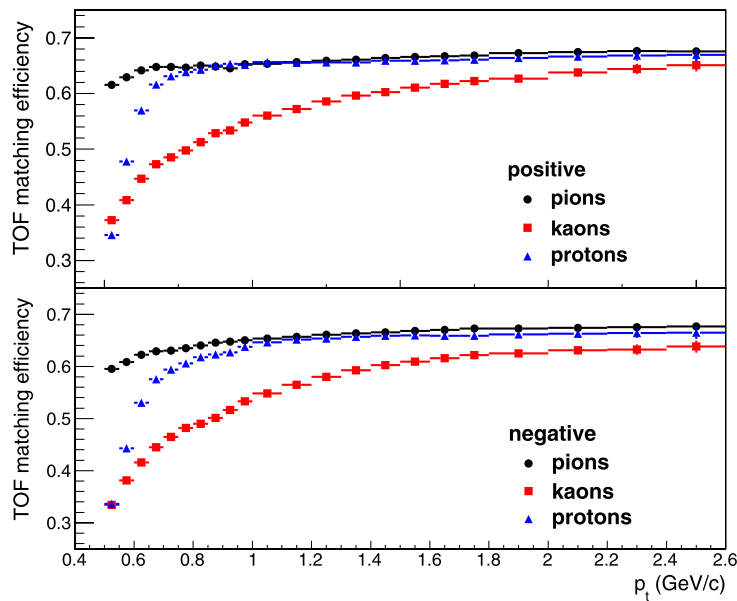
the absorption of particles in the material of the transition radiation detector ($\approx 8\%$).

The TOF matching efficiency has been tested with data, using dE/dx in the TPC to identify the particles. Good agreement between the efficiencies obtained from the data and from Monte-Carlo simulations is observed in case of pions and kaons, with deviations at the level of, at most, 3% and 6% respectively, over the full transverse-momentum range. The observed differences are assigned as systematic errors, see Table 3. In the case of protons and antiprotons, larger differences are observed at p_t below 0.7 GeV/c, where the efficiency varies very rapidly with momentum. This region is therefore not considered in the final results (see Table 3).

Other sources of systematic errors related to the TOF PID procedure have been estimated from Monte-Carlo simulations and cross-checked with data. They include the effect of the residual contribution from tracks wrongly associated with TOF signals, and the quality and stability of the fit procedure used for extracting the yields. Table 3 summarizes the maximal value of the systematic errors observed over the full transverse momentum range relevant in the analysis, for each of the sources mentioned above.

2.6 Kaon identification using their decay within the TPC

In this section, the determination of the yields of charged kaons identified by their weak decay (kink topology) inside the TPC detector is described. These tracks are rejected in the previously described TPC analysis. This procedure allows an extension of the study of kaons to intermediate momenta, on a track-by-track level, although in this analysis the p_t reach is limited by statistics.

Table 3 Summary of systematic errors in the TOF analysis

Systematic errors	$\pi^\pm$	$K^\pm$	p and $\bar{p}$
TOF matching efficiency	<3%	<6%	<4% ($p_t > 1$ GeV/c) <7.5% ($p_t = 0.7$ GeV/c)
PID procedure	<2%	<7%	<3%

The kinematics of the kink topology, measured as a secondary vertex with one mother and one daughter track of the same charge, allows the separation of kaon decays from the main source of background kinks coming from charged pion decays. The decay channels with the highest branching ratio (B.R.) for kaons are the two-body decays

(1) $K^\pm \rightarrow \mu^\pm + \nu_\mu$ (B.R. 63.55%)
(2) $K^\pm \rightarrow \pi^\pm + \pi^0$ (B.R. 20.66%)

Three-body decays with one charged daughter track (B.R. 9.87%) as well as three-body decays into three charged pions (B.R. 5.6%) are also detected.

The algorithm for reconstructing kinks as secondary vertices is applied inside a fiducial volume of the TPC with radius 120 cm $< R <$ 210 cm in order to have a minimum number of clusters for reconstructing both the mother and daughter tracks. Inside this volume a sufficient number of kinks can be found since the $c\tau$ of kaon and pion decays are 3.7 m and 7.8 m, respectively. The mother track of the kink has been selected with similar criteria to those of the TPC tracks used for the dE/dx analysis, except that the minimum required number of clusters per track is 30, because the kink mother track does not traverse the entire TPC. The

relation between the number of clusters per mother track and the radius R of the kink is used as a quality check of the kink reconstruction procedure.

The identification of kaons from kink topology and its separation from pion decay is based on the decay kinematics. The transverse momentum of the daughter with respect to the mother's direction, q_t, has an upper limit of 236 MeV/c for kaons and 30 MeV/c for pions for the two-body decay to $\mu + \nu_\mu$. The corresponding upper limit for the two-body decay (2) $K \to \pi + \pi^0$ is 205 MeV/c. All three limits can be seen as peaks in Fig. 10(a), which shows the q_t distribution of all measured kinks inside the selected volume and rapidity range $|y| < 0.7$. Selecting kinks with $q_t > 40$ MeV/c removes the majority of π-decays as shown by the dashed (before) and solid (after) histograms.

The invariant mass for the decay into $\mu^\pm + \nu_\mu$ is calculated from the measured difference between the mother and daughter momentum, their decay angle, assuming zero mass for the neutrino. Figure 10(b) shows the invariant mass for the full sample of kinks (dashed line) and for the sample after applying the preceding cuts (full line). The masses of pions and kaons are reconstructed at their nominal values. The third peak at 0.43 GeV/c originates from the $K \to \pi + \pi^0$ decay for which the invariant mass is calculated with wrong mass assumptions for the daughter tracks. The broad structure originates from three-body decays of kaons.

At this stage, we have a rather clean sample of kaons as demonstrated in Fig. 10(c) showing the dE/dx vs. the mother momentum. Most of the tracks are within a 3.5σ band with respect to the corresponding Bethe-Bloch curve of kaons. The few tracks outside these limits are at momenta below 600 MeV/c (less than 5%) and they have been removed in the last analysis step.

Efficiency and acceptance The total correction factor includes both the acceptance of kinks and their efficiency (reconstruction and identification). The study has been performed for the rapidity interval $|y| < 0.7$, larger than the corresponding rapidity interval for the other studies in order to reduce the statistical errors.

The acceptance is defined as the ratio of weak decays (two- and three-body decays) whose daughters are inside the fiducial volume of the TPC to all kaons inside the same rapidity window (Fig. 11, upper part). It essentially reflects the decay probability. However, the acceptance is not the same in the low-momentum region for both charges of kaons, since the interaction cross section of the negative kaons with the ITS material is higher than that of the positive kaons. As a result, the acceptance of positive kaons is larger at low momenta.

The efficiency is the ratio of reconstructed and identified kaons divided by the number of kaon decays within the acceptance as shown in Fig. 11 (lower part), as a function of
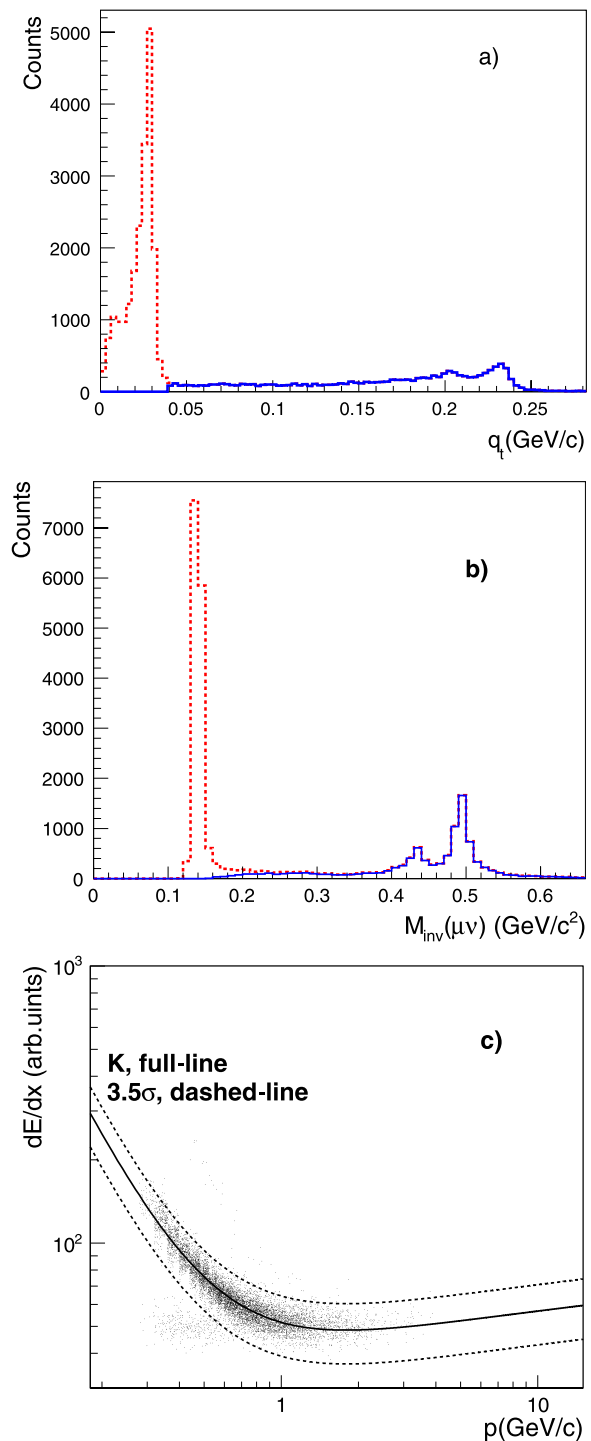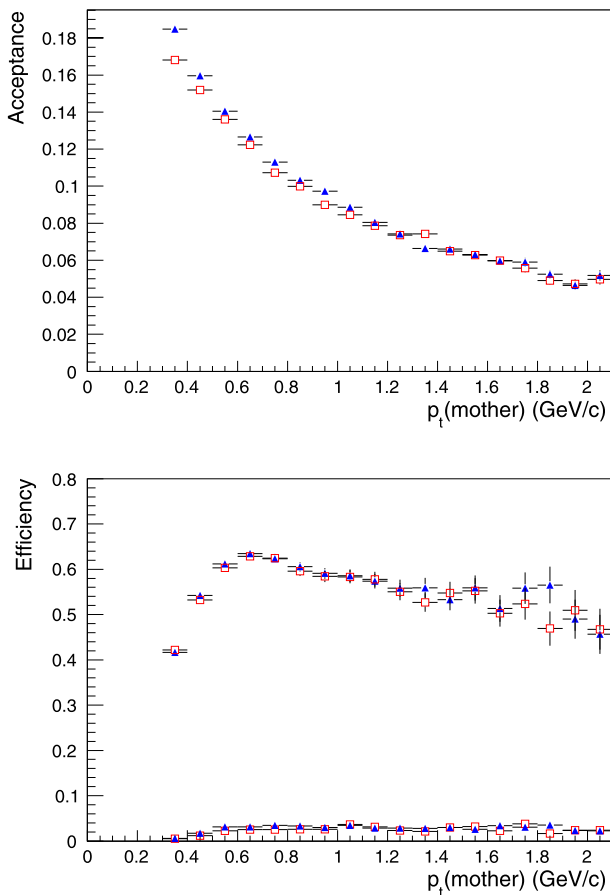

Fig. 10 (Color online) **a** q_t distribution of the daughter tracks with respect to mother momentum for all reconstructed kinks inside the analyzed sample. The *dashed* (*solid*) histograms show the distribution before (after) applying the $q_t > 40$ MeV/c cut. **b** Invariant mass of the two-body decays $K^\pm/\pi^\pm \to \mu^\pm + \nu_\mu$ for candidate kaon kinks. *Solid curve*: after applying $q_t > 40$ MeV/c; *dashed curve*: without this selection (hence also showing the pion decays). **c** dE/dx of kinks as a function of the mother momentum, after applying the full list of selection criteria for their identification

the kaon p_t. It reaches about 60% at 0.7 GeV/c and decreases gradually at higher transverse momenta, as the angle between mother and daughter tracks becomes smaller. The decay angle of kaon kinks allows their identification up to high momenta, e.g. at p_t of 5 GeV/c the values are between 2° and 15°.

The contamination due to random associations of primary and secondary charged tracks has been established using Monte-Carlo simulations and it is systematically smaller than 5% in the studied p_t-range as also shown in Fig. 11. Hadronic interactions are the main source of these fake kinks (65%).

The systematic error due to the uncertainty in the material budget is about 1% as for the TPC analysis. The quality cuts remove about 8% of all real kaon kinks, which leads to a systematic error of less than 1%. The main uncertainty

originates from the efficiency of the kink finding algorithm which has an uncertainty of 5%.

3 Results

Figure 12 shows a comparison between the results from the different analyses. The spectra are normalized to inelastic collisions, as explained in Sect. 2.2. The kaon spectra obtained with various techniques, including K_s^0 spectra [24],

Fig. 11 (Color online) *Upper panel*: The acceptance of kaons decaying in the fiducial volume of the TPC as a function of the kaon p_t for K$^+$ (*full-triangles*) and K$^-$ (*open-squares*). *Lower panel*: The efficiency of reconstructed kaons from kinks as a function of the p_t (mother), separately for K$^+$ (*full-triangles*) and K$^-$ (*open-squares*). The contamination from wrongly associated kinks is also plotted for both charges (lower set of points)

Fig. 12 (Color online) Transverse momentum spectra d^2N/(dp_tdy) for $|y| < 0.5$ of positive (*upper part*) and negative (*lower part*) hadrons from the various analyses. Only systematic errors are plotted

are compared in Fig. 13. The very good agreement demonstrates that all the relevant efficiencies are well reproduced by the detector simulation.
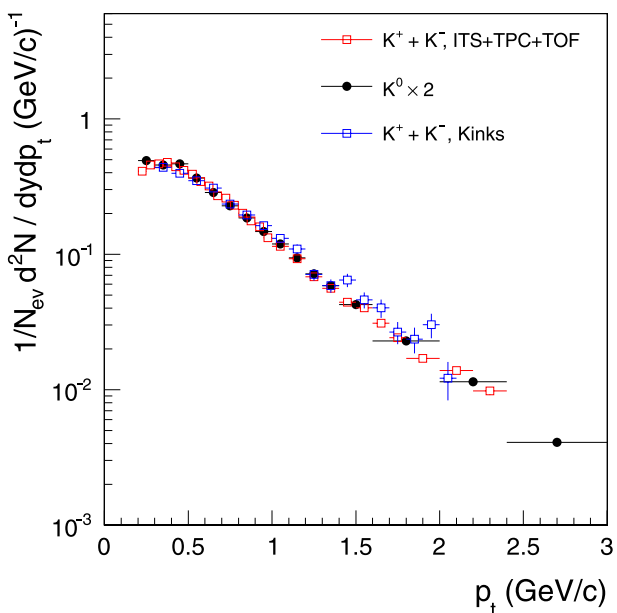
The spectra from ITS stand-alone, TPC and TOF are combined in order to cover the full momentum range. The analyses from the different detectors use a slightly different sample of tracks and have largely independent systematics (mainly coming from the PID method and the contamination from secondaries). The spectra have been averaged, using the systematic errors as weights. From this weighted average, the combined, p_t-dependent, systematic error is derived. The combined spectra have an additional overall normalization error, coming primarily from the uncertainty on the material budget (3%, Sect. 2.5) and from the normalization procedure (2%, Sect. 2.2).

The combined spectra shown in Fig. 14 are fitted with the Lévy (or Tsallis) function (see e.g. [26, 27])

$$\frac{d^2N}{dp_t dy} = p_t \frac{dN}{dy} \frac{(n-1)(n-2)}{nC(nC + m_0(n-2))} \left(1 + \frac{m_t - m_0}{nC}\right)^{-n} \quad (2)$$

with the fit parameters C, n and the yield dN/dy. This function gives a good description of the spectra and has been used to extract the total yields and the $\langle p_t \rangle$, summarized in Table 4. The χ^2/degree-of-freedom is calculated using the total error. Due to residual correlations in the point-by-point systematic error, the values are less than 1. Also listed are the lowest measured p_t-bin and the fraction of the yield contained in the extrapolation of the spectra to zero momen-

tum. The extrapolation to infinite momentum gives a negligible contribution. The systematic errors take into account the contributions from the individual detectors, propagated to the combined spectra, the overall normalization error and the uncertainty in the extrapolation. The latter is evaluated using different fit functions (modified Hagedorn [28] and the UA1 parametrization [29]) or using a Monte-Carlo generator, matched to the data for $p_t < 1$ GeV/c (PYTHIA [15], with tunes D6T [16], CSC and Perugia0 [30], or PHO-

Fig. 14 (Color online) Transverse momentum spectra of positive (*top*) and negative (*bottom*) hadrons from pp collisions at $\sqrt{s} = 900$ GeV. Grey bands: total p_t-dependent error (systematic plus statistical); normalization systematic error (3.6%) not shown. The curves represent fits using a Lévy function

Fig. 13 (Color online) Comparison of charged kaon spectra, obtained from the combined ITS stand-alone, TPC, TOF analysis, from the kink topology and K_s^0 spectra from Ref. [24]. Only statistical errors are shown

Table 4 Integrated yield dN/dy ($|y| < 0.5$) with statistical and systematic errors, and $\langle p_t \rangle$, as obtained from the fit with the Lévy function together with the lowest p_t experimentally accessible, the fraction of extrapolated yield and the χ^2/ndf of the fit (see text). The systematic error of dN/dy and of the $\langle p_t \rangle$ includes the contributions from the systematic errors of the individual detectors, from the choice of the functional form for extrapolation and from the absolute normalization

Particle	dN/dy	$\langle p_t \rangle$ (GeV/c)	Lowest p_t (GeV/c)	Extrapolation	χ^2/ndf
π^+	$1.493 \pm 0.004 \pm 0.074$	$0.404 \pm 0.001 \pm 0.02$	0.10	10%	14.23/30
π^-	$1.485 \pm 0.004 \pm 0.074$	$0.404 \pm 0.001 \pm 0.02$	0.10	10%	12.46/30
K^+	$0.183 \pm 0.004 \pm 0.015$	$0.658 \pm 0.006 \pm 0.05$	0.20	13%	12.71/24
K^-	$0.182 \pm 0.004 \pm 0.015$	$0.642 \pm 0.006 \pm 0.05$	0.20	13%	6.23/24
p	$0.083 \pm 0.002 \pm 0.006$	$0.768 \pm 0.008 \pm 0.06$	0.35	21%	13.79/21
$\bar{\text{p}}$	$0.079 \pm 0.002 \pm 0.006$	$0.760 \pm 0.008 \pm 0.06$	0.35	21%	13.46/21

Table 5 Results of the Lévy fits to combined positive and negative spectra. See text and the caption of Table 4 for details on the systematic errors

Particle	dN/dy	C (GeV)	n	$\langle p_t \rangle$ (GeV/c)	χ^2/ndf
$\pi^+ + \pi^-$	$2.977 \pm 0.007 \pm 0.15$	$0.126 \pm 0.0005 \pm 0.001$	$7.82 \pm 0.06 \pm 0.1$	$0.404 \pm 0.001 \pm 0.02$	19.69/30
$K^+ + K^-$	$0.366 \pm 0.006 \pm 0.03$	$0.160 \pm 0.003 \pm 0.005$	$6.08 \pm 0.2 \pm 0.4$	$0.651 \pm 0.004 \pm 0.05$	8.46/24
$p + \bar{p}$	$0.162 \pm 0.003 \pm 0.012$	$0.184 \pm 0.005 \pm 0.007$	$7.5 \pm 0.7 \pm 0.9$	$0.764 \pm 0.005 \pm 0.07$	15.70/21

JET [18]). While none of these alternative extrapolations provides a description as good as the one from the Lévy fit, we estimate from this procedure an uncertainty of about 25% of the extrapolated part of the yield.

The ratios of π^+/π^- and K^+/K^- as a function of p_t are close to unity within the errors, allowing the combination of both spectra in the Lévy fits. The $\bar{p}/p$ ratio as a function of p_t has been studied with high precision in our previous publication [22]. It is p_t-independent with a mean value of $0.957 \pm 0.006(\text{stat}) \pm 0.014(\text{syst})$. Also here we used the sum of both charges. Table 5 summarizes the fit parameters along with the yields and mean p_t. The errors have been determined as for the individual fits.

Our values on yield and $\langle p_t \rangle$ given in Tables 4 and 5 agree well with the results from $\bar{p}p$ collisions at the same $\sqrt{s}$ [31]. Figure 15 compares the $\langle p_t \rangle$ with measurements in pp collisions at $\sqrt{s} = 200$ GeV [32, 33] and in $\bar{p}p$ reactions at $\sqrt{s} = 900$ GeV [31]. The mean p_t rises very little with increasing $\sqrt{s}$ despite the fact that the spectral shape clearly shows an increasing contribution from hard processes. It was already observed at RHIC that the increase in mean p_t at $\sqrt{s} = 200$ GeV compared to studies at $\sqrt{s} = 25$ GeV is small. The values obtained in pp collisions are lower than those for central Au+Au reactions at $\sqrt{s} = 200$ GeV [32].

The spectra presented in this paper are normalized to inelastic events. In a similar study by the STAR Collaboration the yields have been normalized to NSD collisions [32]. In order to compare these two results, the yields in Table 4 have been scaled to NSD events, multiplying by 1.185 (see Sect. 2.2). The yields of pions increase from $\sqrt{s} = 200$ GeV to 900 GeV by 23%, while K^+ rises by 45% and K^- by 48%.
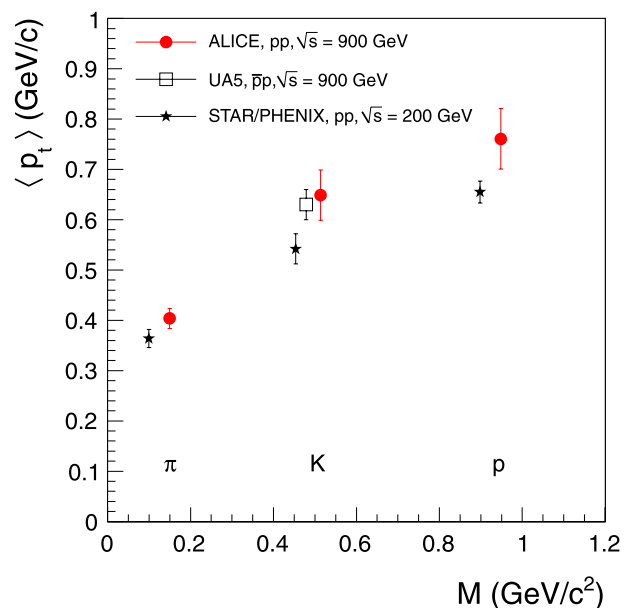
Fig. 15 (Color online) Mean p_t as a function of the mass of the emitted particle in pp collisions at 900 GeV (ALICE, *red solid circles*, statistical and systematic errors) compared to results at $\sqrt{s} = 200$ GeV (*star markers*, average values of the results from the STAR and the PHENIX Collaborations [32, 33]) and $\bar{p}p$ reactions at $\sqrt{s} = 900$ GeV [31] (*open squares*). Some data points are displaced for clarity

Figure 16 shows the K/π ratio as a function of $\sqrt{s}$ both in pp (full symbols, [32, 34, 35]) and in $\bar{p}p$ (open symbols, [36–38]) collisions. For most energies, $(K^+ + K^-)/(\pi^+ + \pi^-)$ is plotted, but for some cases only neutral
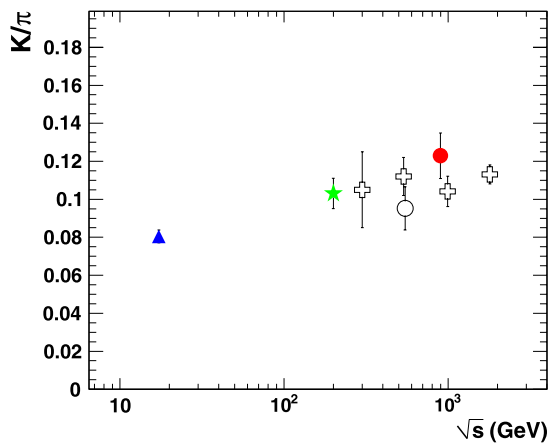
Fig. 16 (Color online) Ratios $(K^+ + K^-)/(\pi^+ + \pi^-)$ and K^0/π as a function of $\sqrt{s}$. Data (*full symbols*) are from pp collisions, (at $\sqrt{s} = 17.9$ GeV by NA49 [34, 35], at $\sqrt{s} = 200$ GeV by STAR [32] and at $\sqrt{s} = 900$ ALICE, present work) and (*open symbols*) from $\bar{p}p$ interaction (at $\sqrt{s} = 560$ GeV by UA5 [37] and at the TEVATRON by E735 [36, 38])

mesons were measured and K^0/π^0 is used instead. The p_t-integrated $(K^+ + K^-)/(\pi^+ + \pi^-)$ ratio shows a slight increase from $\sqrt{s} = 200$ GeV ($K/\pi = 0.103 \pm 0.008$) to $\sqrt{s} = 900$ GeV ($K/\pi = 0.123 \pm 0.004 \pm 0.010$) [32], yet consistent within the error bars. The results at 7 TeV will show whether the K/π ratio keeps rising slowly as a function of $\sqrt{s}$ or saturates.

Protons and antiprotons in Table 4 have been corrected for feed down (mainly from Λ), while the results from the STAR Collaboration are not. The proton spectra measured by PHENIX, on the other hand, have a lower p_t-cut of 0.6 GeV/c. This makes a direct comparison with RHIC data difficult.

Figure 17 shows a comparison of the measured pion, kaon and proton spectra with several tunes of the PYTHIA event generator [15] and with PHOJET [18]. The PYTHIA CSC 306 [39] tune provides a very poor description of the particle spectra for all species. Similar deviations were already seen for the unidentified charged hadron spectra [13]. The other PYTHIA tunes, Perugia0 [30] and D6T [16], and PHOJET give a reasonable description of the charged pion spectra, but show large deviations in the kaon and proton spectra. The measured kaon p_t-spectrum falls more slowly with increasing p_t than the event generators predict. A similar trend is seen for the proton spectra, except for PYTHIA tune D6T, which describes the proton spectra reasonably well.

The upper panel of Fig. 18 shows the p_t-dependence of the K/π and also the measurements by the E735 [36] and STAR Collaborations [32]. It can be seen that the observed increase of K/π with p_t does not depend strongly on collision energy.
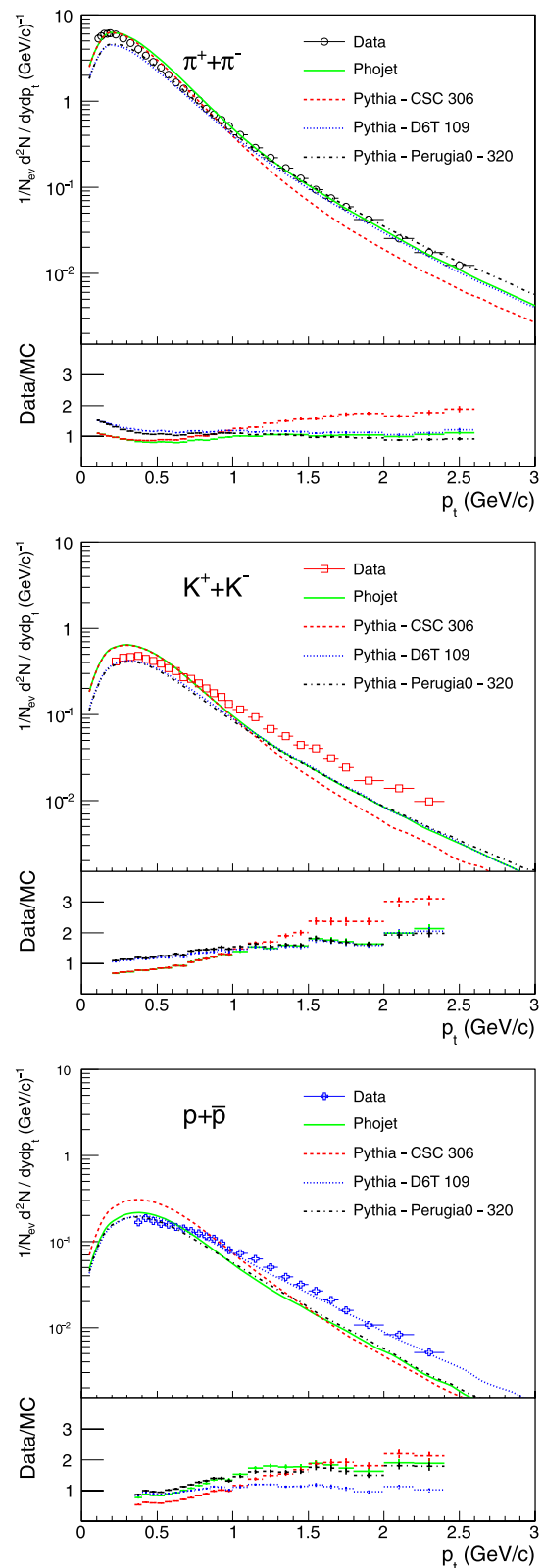
Fig. 17 (Color online) Comparison of measured pion, kaon and proton spectra at $\sqrt{s} = 900$ GeV (both charges combined) with various tunes of event generators. Statistical errors only. See text for details
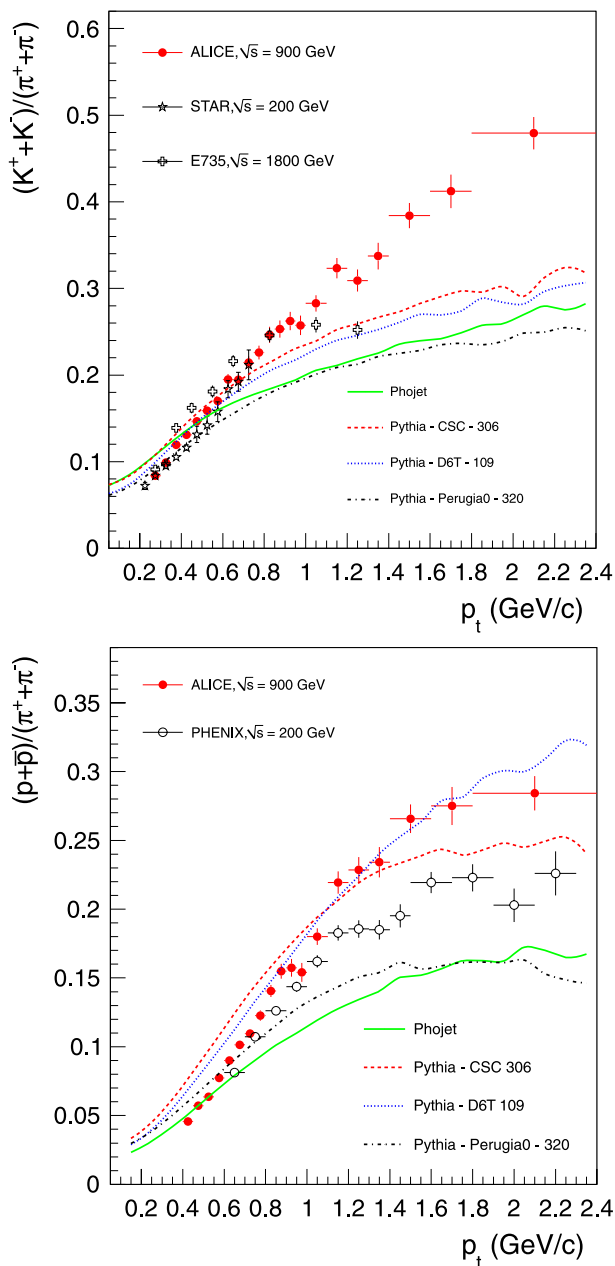
Fig. 18 (Color online) Ratios of $(K^+ + K^-)/(\pi^+ + \pi^-)$ (*upper panel*) and $(p + \bar{p})/(\pi^+ + \pi^-)$ (*lower panel*) as a function of p_t from pp collisions at $\sqrt{s} = 900$ GeV (statistical errors only). Values from the E735 Collaboration [36] and the STAR Collaboration [32] (*upper part*) and from the PHENIX Collaboration [41] (*lower part*) also are given. The *dashed* and *dotted* curves refer to calculations using PYTHIA and PHOJET at $\sqrt{s} = 900$ GeV

A comparison with event generators shows that at $p_t > 1.2$ GeV/c, the measured K/π ratio is larger than any of the model predictions. It is interesting to note that while the spectra in the CSC tune are much steeper than the other tunes, the p_t-dependence of the K/π ratio is very similar. In

the models, the amount of strangeness production depends on the production ratios of gluons and the different quark flavours in the hard scattering and on the strangeness suppression in the string breaking. The latter could probably be tuned to better describe the data. A similar disagreement between measured strangeness production and PYTHIA predictions was found at RHIC energies [40].

In the bottom panel of Fig. 18, the measured p/π ratio is compared to results at $\sqrt{s} = 200$ GeV from the PHENIX Collaboration [41]. Both measurements are feed-down corrected. At low p_t, there is no energy-dependence of the p/π ratio visible, while at higher $p_t > 1$ GeV/c, the p/π ratio is larger at $\sqrt{s} = 900$ GeV than at $\sqrt{s} = 200$ GeV energy.

Event generators seem to separate into two groups, one with high p/π ratio (PYTHIA CSC and D6T), which agree better with the data and one group with a lower p/π ratio (PHOJET and PYTHIA Perugia0), which are clearly below the measured values. These comparisons can be used for future tunes of baryon production in the event generators.

4 Summary

We present the first analysis of transverse momentum spectra of identified hadrons, π^+, π^-, K^+, K^-, p, and $\bar{p}$ in pp collisions at $\sqrt{s} = 900$ GeV with the ALICE detector. The identification has been performed using the dE/dx of the inner silicon tracker, the dE/dx in the gas of the TPC, the kink topology of the decaying kaons inside the TPC and the time-of-flight information from TOF. The combination of these techniques allows us to cover a broad range of momentum.

Agreement in the K/π ratio is seen when comparing to $\bar{p}p$ collisions at the Tevatron and Sp$\bar{p}$S. Comparing our results with a similar measurement from the STAR Collaboration using pp collisions at $\sqrt{s} = 200$ GeV the shape of the spectra shows an increase of the hard component, but we observe only a slight increase of the mean p_t-values. Whether the fraction of strange to non-strange particles rises with increasing $\sqrt{s}$ remains open until data at 7 TeV become available.

References

1. B. Alessandro et al. (ALICE Collaboration), J. Phys. G **32**, 1295 (2006)
2. M. Cinausero et al. (ALICE Collaboration), J. Phys. G **30**, 1517 (2004)
3. K. Aamodt et al. (ALICE Collaboration), J. Instrum. **3**, S08002 (2008)
4. G. Aglieri Rinella, A. Kluge, M. Krivda (ALICE Collaboration), J. Instrum. **2**, P01007 (2007)
5. B. Alessandro et al., J. Instrum. **5**, P02008 (2010). arXiv:1001.2276
6. K. Aamodt et al. (ALICE Collaboration), J. Instrum. **5**, P03003 (2010). arXiv:1001.0502
7. J. Alme et al., Nucl. Instrum. Methods Phys. Res. A **622**, 316 (2010). arXiv:1001.1950
8. A. Akindinov et al., Nuovo Cimento B **124**, 235 (2009)
9. A. Akindinov et al., Nucl. Instrum. Methods Phys. Res. A **572**, 676 (2007). arXiv:physics/0612083
10. A. Akindinov et al., Nucl. Instrum. Methods Phys. Res. A **615**, 37 (2010)
11. A. Akindinov et al., Eur. Phys. J. C **68**, 601 (2010)
12. K. Aamodt et al. (ALICE Collaboration), Eur. Phys. J. C **68**, 89 (2010). arXiv:1004.3034
13. K. Aamodt et al. (ALICE Collaboration), Phys. Lett. B **693**, 53 (2010). arXiv:1007.0719
14. R.E. Ansorge et al. (UA5 Collaboration), Z. Phys. C **33**, 175 (1986)
15. T. Sjostrand, S. Mrenna, P.Z. Skands, J. High Energy Phys. **05**, 026 (2006)
16. M.G. Albrow et al. (Tev4LHC QCD Working group), arXiv:hep-ph/0610012
17. R. Brun, F. Carminati, S. Giani, CERN-W5013
18. R. Engel, J. Ranft, S. Roesler, Phys. Rev. D **52**, 1459 (1995)
19. G. Bendiscioli, D. Kharzeev, Riv. Nuovo Cimento **17N6**, 1 (1994)
20. Y.-S. Zhang, Y.-G. Li, J.-F. Liu et al., Phys. Rev. C **54**, 332 (1996)
21. E. Klempt, F. Bradamante, A. Martin et al., Phys. Rep. **368**, 119 (2002)
22. K. Aamodt et al. (ALICE Collaboration), Phys. Rev. Lett. **105**, 072002 (2010). arXiv:1006.5432
23. B.B. Back et al. (PHOBOS Collaboration), Phys. Rev. C **75**, 024910 (2007). arXiv:nucl-ex/0610001
24. K. Aamodt et al. (ALICE Collaboration), Eur. Phys. J. C **71**, 1594 (2011)
25. W. Blum, W. Riegler, L. Rolandi, *Particle Detection with Drift Chambers*, 2nd edn. (Springer, Berlin, 2008)
26. C. Tsallis, J. Stat. Phys. **52**, 479 (1988)
27. B.I. Abelev et al. (STAR Collaboration), Phys. Rev. C **75**, 064901 (2007). arXiv:nucl-ex/0607033
28. R. Hagedorn, Riv. Nuovo Cimento **6N10**, 1 (1984)
29. C. Albajar et al. (UA1 Collaboration), Nucl. Phys. B **335**, 261 (1990)
30. P.Z. Skands, Contribution to the 1st International Workshop on Multiple Partonic Interactions at the LHC, Perugia, Italy, Oct. 2008, Fermilab-Conf-09-113-T, arXiv:0905.3418 [hep-ph] and arXiv:1005.3457 [hep-ph]
31. R.E. Ansorge et al. (UA5 Collaboration), Phys. Lett. B **199**, 311 (1987)
32. B.I. Abelev et al. (STAR Collaboration), Phys. Rev. C **79**, 034909 (2009). arXiv:0808.2041
33. A. Adare et al. (PHENIX Collaboration), 2010. arXiv:1005.3674
34. C. Alt et al. (NA49 Collaboration), Eur. Phys. J. C **45**, 343 (2006). arXiv:hep-ex/0510009
35. T. Anticic et al. (NA49 Collaboration), Eur. Phys. J. C **68**, 1 (2010). arXiv:1004.1889
36. T. Alexopoulos et al. (E735 Collaboration), Phys. Rev. D **48**, 984 (1993)
37. G.J. Alner et al. (UA5 Collaboration), Nucl. Phys. B **258**, 505 (1985)
38. T. Alexopoulos et al., Phys. Rev. D **46**, 2773 (1992)
39. A. Moraes (ATLAS Collaboration), ATLAS Note ATL-COM-PHYS-2009-119, 2009
40. M. Heinz, Eur. Phys. J. C **49**, 129 (2007). arXiv:0707.1508
41. S.S. Adler et al. (PHENIX Collaboration), Phys. Rev. C **74**, 024904 (2006). arXiv:nucl-ex/0603010